

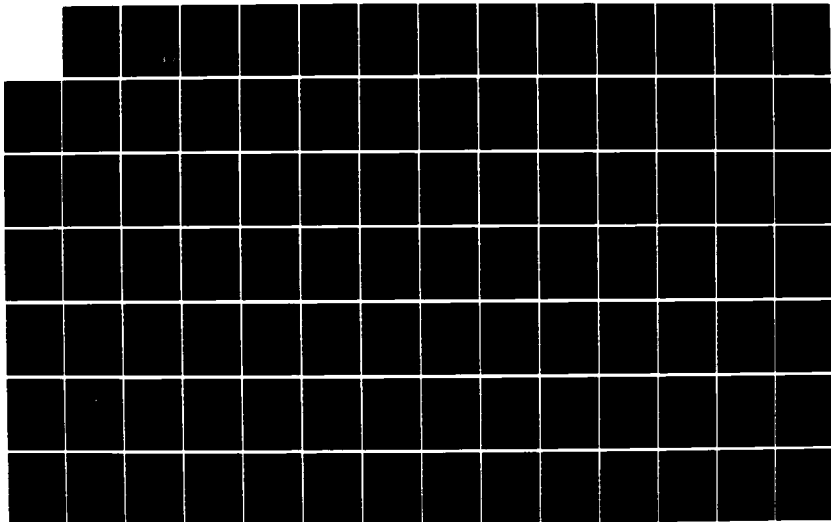
AD-A163 965

COMPARISON OF BACKGROUND CHARACTERISTICS OF AN RCS
(RADAR CROSS SECTION). (U) AIR FORCE INST OF TECH
WRIGHT-PATTERSON AFB OH SCHOOL OF ENGI.. G R SIMPSON
DEC 85 AFIT/GE/ENG/85D-40 F/G 17/9

1/2

UNCLASSIFIED

NL





MICROCOPY RESOLUTION TEST CHART
NATIONAL BUREAU OF STANDARDS 1963-A

AD-A163 965



COMPARISON OF BACKGROUND CHARACTERISTICS OF AN
RCS MEASUREMENT RANGE USING A CW-MULLING
TECHNIQUE AND A PULSE-GATING TECHNIQUE

THESIS

George R. Simpson
First Lieutenant, USAF

AFIT/GE/ENG/85D-40

This document has been approved
for public release and sale; its
distribution is unlimited.

DEPARTMENT OF THE AIR FORCE
AIR UNIVERSITY

AIR FORCE INSTITUTE OF TECHNOLOGY

Wright-Patterson Air Force Base, Ohio

DTIC
ELECTE
FEB 13 1986
S A D

DTIC FILE COPY

°6 2 1 2 086

1

AFIT/GE/ENG/85

**COMPARISON OF BACKGROUND CHARACTERISTICS OF AN
RCS MEASUREMENT RANGE USING A CW-NULLING
TECHNIQUE AND A PULSE-GATING TECHNIQUE**

THESIS

George R. Simpson
First Lieutenant, USAF

AFIT/GE/ENG/85D-40

DTIC
ELECTE
FEB 13 1986
A

Approved for public release; distribution unlimited

AFIT/GE/ENG/85D-40

COMPARISON OF BACKGROUND CHARACTERISTICS OF AN RCS MEASUREMENT
RANGE USING A CW-NULLING TECHNIQUE AND A PULSE-GATING TECHNIQUE

THESIS

Presented to the Faculty of the School of Engineering
of the Air Force Institute of Technology

Air University

In Partial Fulfillment of the
Requirements for the Degree of
Master of Science in Electrical Engineering

George R. Simpson, B.S.E.E.
First Lieutenant, USAF

December 1985

Approved for public release; distribution unlimited

ACKNOWLEDGMENT

It has been more than one year since I began working on this thesis project and I have had much help, advice, and encouragement from others. I feel indebted to and appreciative of my thesis sponsor, Dr. Brian M. Kent, for his unending patience and guidance during my times of need. I am also indebted to 1Lt. R. J. Jost, my thesis advisor, for his many helpful discussions and encouragement he provided me throughout this work. A very special word of thanks is owed to Mr. Jim Kelly, formerly of AFWAL, for sharing with me his hard-earned insight into the wide array of equipment and techniques used in this thesis. Finally, I wish to thank my wife Karin for her patience and understanding during this entire 18 month period, for without her my life would be empty. But I dedicate all of this effort to my three sons; George, Andrew, and Patrick; in the hope that they might understand the true meaning and value of education much sooner in their lives than did I.

George R. Simpson



Accession For	
NTIS	<input checked="" type="checkbox"/>
DTIC	<input type="checkbox"/>
Unannounced	<input type="checkbox"/>
Justification	
By	
Date	
Approved	
Signature	
Post	

A1

Table of Contents

Acknowledgments.....	ii
List of Figures.....	iv
List of Tables.....	vii
Abstract.....	viii
I. Introduction.....	1
Introduction.....	1
Background.....	3
II. Theoretical Considerations.....	7
Clutter Considerations.....	7
System Sensitivity and Noise Figure Considerations.....	11
III. Systems Performance Analysis.....	16
Idealized CW-Nulling System.....	18
Idealized Pulse-Gating System.....	22
Modification of Idealized CW-Nulling System.....	32
Modification of Idealized Pulse-Gating System.....	35
Additional Comments and Comparisons.....	38
S-Band Monostatic System.....	41
IV. Comparison of Background Characteristics.....	47
Time Domain Comparison of Chamber Background Characteristics....	47
Fixed Frequency RCS Pattern Comparisons.....	57
V. Conclusions and Recommendations.....	72
Conclusions.....	72
Recommendations.....	73
Appendix A: Stepped Frequency/Time Domain Measurements.....	77
Appendix B: Fundamental Mode Mixing.....	84
Appendix C: Some Comments on Differences Between the Compact Range and the Far-Field Range.....	88
Bibliography.....	95
Vita.....	97

List of Figures

Figure		Page
3.1	Simplified Diagram of Far-Field Chamber With Generic RCS Measurement System.....	17
3.2	Simplified Diagram of CW-Nulling System.....	17
3.3	Simplified Diagram of Pulse-Gating System.....	23
3.4	Block Diagram of Pulse-Gating Units.....	24
3.5	Frequency Spectra at Points Highlighted in Figure 3.3 and Figure 3.6.....	25-26
3.6	Simplified Block Diagram of SA 1750 Receiver.....	30
3.7	Detailed Diagram of CW-Nulling System.....	33
3.8	Detailed Diagram of Pulse-Gating System.....	36
3.9	Simplified Diagram of S-Band, Single Antenna CW-Nulling System Using Magic-Tee/Balancing Arm.....	42
3.10	Simplified Diagram of S-Band, Single Antenna Pulse-Gating System	44
3.11	Illustrative Spectral Diagram of Switching Transient Relative to Direct RF Signal.....	45
4.1	Cross-Sectional Diagram of Cone-Sphere Target Shape Used in Time Domain and Fixed Frequency Measurements.....	48
4.2	CW Time Domain Response: 8 Inch Sphere Mounted on Low RCS Pedestal.....	50
4.3	CW Time Domain Response: First Background Scan With No Target Present.....	50
4.4	CW Time Domain Response: 8 Inch Sphere Minus First Background.....	52
4.5	CW Time Domain Response: Second Background Minus First Background.....	52
4.6	CW Time Domain Response: Low RCS Cone-Sphere Mounted on Target Pedestal.....	53

4.7	CW Time Domain Response: Expanded View of Figure 4.6.....	53
4.8	CW Time Domain Response: Third Background Scan With No Target Present.....	55
4.9	CW Time Domain Response: Cone-Sphere Minus Third Background.....	55
4.10	Pulse-Gated Time Domain Response: 8 Inch Sphere Mounted on Target Pedestal.....	56
4.11	Pulse-Gated Time Domain Response: Pulsed Background Scan With No Target Present.....	56
4.12	CW-Nulling and Pulse-Gating Measurements of a 12 Inch Square Plate (8.5 GHz, Horizontal Polarization).....	58
4.13	CW-Nulling and Pulse-Gating Measurements of a 12 Inch Cylinder (diameter = 3 inches) (9.37 GHz, Horiz. Pol.).....	60
4.14	CW-Nulling and Pulse-Gating Measurements of a 12 Inch Cylinder (diameter = 3 inches) (11.5 GHz Vert. Pol.).....	61
4.15	CW-Nulling and Pulse-Gating Measurements of a Cone-Sphere (8.5 GHz, Horizontal Polarization).....	62
4.16	CW-Nulling and Pulse-Gating Measurements of a Cone-Sphere (9.37 GHz, Vertical Polarization).....	63
4.17	CW-Nulling and Pulse-Gating Measurements of a Cone-Sphere (15 GHz, Vertical Polarization).....	65
4.18	CW-Nulling and Pulse-Gating Measurements of a Cone-Sphere (18 GHz, Vertical Polarization).....	66
4.19	CW-Nulling and Pulse-Gating Measurements of a Cone-Sphere With a Small Corner Reflector Embedded in Chamber Backwall.	68
4.20	Illustrative Diagram of Far-Field Range Low RCS Support Pedestal and Surrounding Features.....	70
4.21	Illustrative Diagram of New Compact Range Low RCS Support Pedestal and Surrounding Features.....	71
5.1	Hybrid CW-Nulling/Pulse-Gating System.....	76
A.1	Cutaway View of Far-Field Range and a Resultant Time Domain Response Scan.....	80
A.2	Conceptual Time and Frequency Domain Data.....	81

A.3	Sample Results of Transforming Bad Frequency Domain Data Into the Time Domain.....	83
B.1	Simplified Diagram of Fundamental Mode Mixing System.....	85
C.1	Simplified Diagram of Compact Range Geometry.....	89
C.2	Sample Far-Field Antenna Radiation Patterns.....	91
C.3	Sample Compact Range Antenna Amplitude Distribution.....	93

List of Tables

Table		Page
B.1	SA 1750 Receiver Sensitivity Characteristics Due to Harmonic Mixer Front End.....	85

Abstract

This thesis compares the relative performance of a CW-nulling technique versus a pulse-gating technique for radar cross section (RCS) measurements. The purpose is (1) to provide a detailed comparison of these two systems in terms of system noise figure and system losses, and (2) to demonstrate the effectiveness of time-separating the target area from the surrounding chamber when using the pulse-gating technique.

The pulse-gating system is shown to have far superior system noise figure characteristics than the CW-nulling system. Pulse-gating has only a slightly greater system loss due to the added complexity of the pulse modulating and range gating components. The combined effect is that the pulse-gating technique is capable of improving signal-to-noise ratio, thus increasing the reliability of making accurate RCS measurements.

It is also shown that the pulse-gating system reduces the effect of chamber clutter sources. Supporting data in the form of moderate resolution time domain measurements of chamber scattering sources is presented. Supplemental fixed frequency target RCS measurements correlate with the time domain results. For high RCS targets where the target return is the dominant chamber scattering mechanism, the systems perform equally well. However, when the target RCS is of the same order as chamber clutter, the CW-nulling system yields distorted results since it fails to distinguish between target and clutter source return. In contrast, the pulse-gating system eliminates the most significant clutter source returns and produces more accurate RCS patterns.

COMPARISON OF BACKGROUND CHARACTERISTICS OF AN RCS MEASUREMENT RANGE USING A CW-NULLING TECHNIQUE AND A PULSE-GATING TECHNIQUE

I. Introduction and Background

A. Introduction

In an effort to modernize and increase both the efficiency and flexibility of their radar cross section (RCS) measurement capabilities, the Air Force Wright Aeronautical Laboratories (AFWAL) is constructing a compact RCS measurement facility to supplement an existing far-field range. Recall that a far-field range requires a target to be measured in the far-field of the antenna to insure a reasonable approximation of uniform plane wave illumination on the target. This can place severe restrictions on the maximum target size for a limited range (indoor) system. On the other hand, the compact range utilizes the geometric focusing properties of a paraboloidal reflector antenna to create a relatively large plane wave region in the near field of the reflector. This relaxes real estate requirements and allows larger targets to be

measured at higher frequencies since the plane wave region is determined primarily by the size of the reflector. (See Appendix C for more details comparing these two measurement range designs.)

The instrumentation radar system currently in use on the far-field range employs CW cancellation techniques to eliminate background clutter signals to maximize the sensitivity of the measurement system. This background cancellation is performed by using a frequency sensitive circuit to compensate (or null) the clutter returns from the empty anechoic chamber (chamber with no target present). At AFWAL these cancellation circuits are either a "feedthrough nulling loop" or a "magic-tee" balancing arm. After nulling the chamber, the target is placed in the chamber and the measured signal represents the RCS of the target.

Unfortunately, CW-nulling does not perform well when target RCS levels are on the same order of magnitude as chamber clutter sources. Similarly, it will not perform well when large clutter sources are cancelled. In the compact range, the reflector antenna is a very large clutter source. In order to achieve the potential sensitivity benefits of the compact range, this large clutter source must be eliminated or separated from the target return signal. A pulse-gating instrumentation radar system does this by time-separating the target area from the surrounding chamber environment.

In the context of this thesis, a pulse-gating radar is one which first pulse modulates a CW transmitter and then range gates the receiver. The duty cycle of the modulation is typically 15% or less. The range gating technique employs a single adjustable range bin containing only the target area at an a priori known range.

The pulse-gating radar system does not employ feedthrough nulling or balancing circuits and thus has the flexibility to make two different types of RCS measurements. These are the AFWAL standard measurement of fixed frequency RCS versus aspect angle and a new capability of target RCS versus frequency for a fixed aspect angle. This latter measurement is a stepped frequency or time-domain measurement that cannot be performed with the CW-nulling system since it is a frequency sensitive system.

Thus, improvements in RCS measurements are needed because: (1) CW-nulling is too slow and inaccurate for low RCS targets, (2) CW-nulling is incompatible with important stepped frequency techniques, (3) CW-nulling has insufficient clutter rejection for a state-of-the-art RCS data acquisition system. By combining a pulse-gating radar system with the compact range, AFWAL will own a state-of-the-art RCS measurement facility that is more accurate, more sensitive and more flexible than the present CW-nulling/far-field facility.

B. Background

There have been several previous studies in which differences between CW-nulling and pulse-gating have been noted and discussed. Mentzer (1:123) compares and contrasts these two systems. He states that the pulse-gating system is capable of higher signal-to-noise ratios because of higher possible transmit power. A reduction in the amount of clutter that the radar system "sees" is what permits this to be true. Since the CW-nulling system illuminates the entire chamber, any increase in transmitted power would serve only to increase the return from the various chamber clutter sources as well as the target. Thus no improvement in signal-to-

noise would be obtained by raising transmit power in the CW-nulling case.

Bahret (2:26) points out one of the most critical disadvantages of the CW nulling method: the shadowing effect or the change in background illumination when a target is placed in the chamber. This is most important when the target being measured is a highly forward scattering shape usually associated with low monostatic RCS. Blacksmith, Hiatt, and Mack (3:918) also make note of this effect in their classic paper on RCS measurements.

Recently, Tavormina (4) makes a distinction between several different types of pulse radar measurement systems. The first pulse radar system uses a wide bandwidth receiver with a matched filter requiring many spectral components. The other, called the gated CW system, uses a narrow bandwidth (CW) receiver to reject spectral components except for the carrier frequency component. This method of detecting pulsed signals using (essentially) CW receivers has a theoretical basis and is discussed in Peebles as signal recovery by low-pass filtering (5:314). The pulse-gated method discussed in this thesis is based on an updated implementation of the latter technique.

In other recent work, Whitacre (6) discusses the design and development of a pulse-gating radar system used at The Ohio State University compact RCS measurement facility. Prior to his discussion of the pulse-gating technique, Whitacre shows difficulties encountered when OSU attempted to cancel the clutter effects due to the large reflector using the CW-nulling technique. Whitacre's report, however, primarily describes the design factors and procedures used to develop the OSU compact range facility. His investigation did not consider a detailed

signal/system analysis and comparison of the CW-nulling and pulse-gating RCS measurement systems. Walton and Young (7:1222) demonstrate that typical anechoic chamber clutter sources can have greater return signal amplitudes than a 6 inch sphere. They conclude that the system sensitivity limits due to clutter can be reduced by pulse-gating. They further demonstrate that pulse-gating techniques significantly increase the accuracy of the RCS acquisition system for low RCS levels.

It is the purpose of this investigation to supplement Whitacre's investigation with a thorough signal/system analysis and comparison between these two widely employed measurement techniques. In Chapter II, theory relevant to these systems will be discussed. Particularly, the results of a recent AFIT MS Thesis by Link (8) will be shown to support the argument stated by Walton and Young that sensitivity is improved by pulse-gating. Then sensitivity or signal-to-noise equations for later use and comparison will be discussed. In Chapter III the pulse-gating and CW-nulling systems are compared based on the sensitivity equations discussed in Chapter II. These equations will not include the anechoic chamber as a specific contributor of loss, noise or clutter effects beyond the R loss due to target range. In Chapter IV the effect on the systems due to the chamber and all the clutter sources within the chamber is examined and compared. Time domain plots of the chamber will show the relative amplitudes of various scattering sources. Fixed frequency measurements will also be compared and the effect of gating out clutter sources will become evident. In addition, Chapter IV compares and contrasts the actual background characteristics of these two RCS measurement systems. Finally, Chapter V concludes the thesis and presents recommendations for future

investigations. It is followed by three Appendices. Appendix A discusses the underlying theory behind stepped frequency/time domain measurements. This Appendix is included to tutor future AFIT workers so that this useful diagnostic tool can be implemented on the AFIT RCS chamber. Appendix B describes a modified pulse-gating system known as the fundamental mode mixing system. This technique maximizes the sensitivity of the harmonic receiver used in this study. As noted earlier, Appendix C provides a description of the compact range and compares some of its features to those of the far-field range.

II Theoretical Considerations

A. Clutter Considerations

An instrumentation radar system designed to measure the RCS of various targets inside an anechoic chamber must separate the desired signal from unwanted clutter. The "clutter" comes from the multitude of scatterers within the anechoic chamber. Undesired clutter sources include imperfect (or partially reflective) anechoic chamber sidewalls and backwalls, target/support column interactions, direct feed-horn antenna coupling, and so forth. In order to make accurate measurements it is necessary to eliminate or cancel as much of the clutter as possible. The CW-nulling and pulse-gating RCS measurement systems attempt to minimize this "background clutter" by using different techniques. In the case of the CW-nulling system, a cancellation scheme is used. What is cancelled is, in terms of RCS, the RCS of the empty anechoic chamber. RCS, σ , is defined as

$$\sigma = \lim_{R \rightarrow \infty} 4\pi R^2 \left| \frac{E_s^t}{E_i} \right|^2 \quad (2-1)$$

where R is the target range, E_s^t is the electric field scattered from the target, E_i is the electric field incident on the target. If the target is simply the empty anechoic chamber then

$$\sigma = \sigma_c \quad (2-2)$$

Where σ_c is the RCS of the empty chamber, which is what the CW-nulling

system strives to cancel. After the chamber is nulled, the target of interest is placed in the chamber and the CW-nulling system "measures" the RCS of the target, σ_t .

In actuality, the CW-nulling system does a very good job of nulling out the empty chamber RCS. But when the target is introduced into the chamber, the field distributions change from those of the empty chamber because of the presence of this new object. This may range from an imperceptible change such that would be associated with the introduction of a highly specular target, to a vast alteration of what was σ_c with the introduction of a target that scatters significant energy levels in the forward direction. A good example of a highly specular target is a flat plate whereas an example of a high forward scattering target is a cone-sphere. In either case, it is reasonable to expect that the target somehow alters the signal that represented σ_c which was nulled out by the CW-nulling system. What is actually measured in a target RCS measurement is a superposition of the actual target return and the altered clutter return. From Link (8:IV-1,23) the signal received by the radar system can be written as

$$x = y_t + y_c e^{j\phi} . \quad (2-3)$$

Where

ϕ = relative phase difference between y_t and y_c ,
 y_t = amplitude of target return signal,
 y_c = amplitude of clutter return signal.

ion (2-1), y_t has associated with it a cross section σ_t , and y_c

has associated with it a cross section σ_c . Link demonstrates (8:IV-3) that the measured cross section is

$$\sigma_m = |x|^2 = y_t^2 + y_c^2 + 2y_t y_c \cos \phi \quad (2-4)$$

Link's assumptions (8:IV-1,2) leading up to this equation are that y_c is a deterministic signal and that y_t is a signal from a randomly distributed target. The target is considered randomly distributed in the sense that it is a complex association of individual scatterers. It is assumed here that this is a valid model for the general case of a target RCS measurement.

Link then proceeds to derive the probability distribution function (pdf) for the measured cross section, σ_m , as a function of σ_m , σ_c , and the mean of σ_t , $\bar{\sigma}_t$. The result is (8:IV-14)

$$f_m(\sigma_m) = \frac{1}{\bar{\sigma}_t} \exp \left[\frac{-(\sigma_m + \sigma_c)}{\bar{\sigma}_t} \right] I_0 \left(\frac{2\sqrt{\sigma_m \sigma_c}}{\bar{\sigma}_t} \right), \quad \sigma_m > 0 \quad (2-5)$$

where $I_0(x)$ is the modified Bessel function of zero order. This is the Nakagami-Rice distribution function which is the distribution for the instantaneous amplitude of the sum of a constant vector (the clutter cross section σ_c) and a Rayleigh distributed vector (the target RCS σ_t).

What makes this distribution function so remarkable in this study is that as σ_c tends toward zero, the pdf becomes Rayleigh, which was the assumed pdf of the target. Thus it becomes obvious that a key factor in obtaining accurate RCS measurements of a given target is to decrease by as much as possible the cross section of the background clutter σ_c . This

essentially says that an increase in system sensitivity can be realized by decreasing σ_c . Recall the statement by Walton and Young (7:1223) "the sensitivity limits due to clutter can be reduced by a pulse technique which would range gate in real time." This supports the supposition that by using the pulse-gating technique, the sensitivity of an RCS measurement system can be increased, leading to more accurate measurements of a wider variety of targets.

As discussed earlier, the CW nulling system illuminates the entire anechoic chamber. For this case, σ_c takes on some value that actually represents the superposition of the return signals from all of the various chamber clutter sources. Then, without being able to distinguish what the clutter source mechanisms are, σ_c is cancelled by the CW-nulling system to reach the deepest null possible. This null level then becomes the "background" level of the CW chamber. Blacksmith, et al., point out in a specific example that to measure no more than a 5% error in σ_c , the background must be 32 dB below the desired target return signal (3:907,908). Obviously, the CW-nulling system cannot be expected to measure a target with an RCS on the same order as the background simply because the CW-nulling system cannot distinguish such a target from the background.

When operating the pulse-gating radar for measuring target RCS, only a fraction of the anechoic chamber is seen by the radar receiver at any one time. In essence, the radar is given some capability to distinguish between various chamber clutter sources through a time-separation process. If the radar can time-separate the target area from the rest of the chamber environment, then it can eliminate scattering sources that lie

outside of the range bin. Clutter sources that may remain are the target support pedestal, absorber cones covering the sidewalls within the range bin, and any undesirable target/support pedestal interaction that may occur when the target is placed atop the pedestal. If these elements contribute a smaller σ_c than does the entire chamber (as in the CW illumination case), then an increase in system sensitivity can be expected when operating pulse-gated as opposed to CW nulling. If this is indeed the case, then the background level for the pulse-gated RCS measurement system would be lower than that for the CW-nulling RCS measurement system. Based on these arguments, the pulse-gating system would have greater sensitivity to make more accurate measurements of even low RCS targets.

B. System Sensitivity and Noise Figure Considerations

Analysis involving sensitivity and noise figure in communication systems is rather straightforward and has been presented by many authors (for instance 5,9). From the radar system point of view, RCS is a parameter in the well known radar range equation (9:4). In the radar range equation, σ is treated as a representative value for the target in question, a mean or expected value. In the typical application of the radar equation the parameter being sought is usually the target range R for some probability of detection and probability of false alarm. In the instrumentation radar systems being studied in this thesis, the range is fixed and the parameter of interest is the cross section σ . Thus we can rearrange the definition of the minimum detectable signal, S_{min} to become

$$S_{min} = \frac{P_t G^2 \lambda^2 \sigma_{min}}{(4\pi)^3 R^4} \quad (2-6)$$

where P_t = transmitter output power
 G = transmit antenna gain = receive antenna gain
 λ = wavelength
 σ_{min} = minimum measurable RCS

A more fundamental definition of S_{min} comes from the consideration of the noise power received by the receiver. This definition is from Skolnik (9:19)

$$S_{min} = k T_o B_n F_n \left(\frac{S_o}{N_o} \right)_{min} \quad (2-7)$$

where k = Boltzmann's constant = 1.38×10^{-23} J/K
 T_o = standard temperature = 290°K
 B_n = receiver effective noise bandwidth
 F_n = receiver noise figure

For a receiving system including the receive antenna, transmission lines and other components external to the actual receiver, equation (2-7) becomes

$$S_{min} = k T_o B_n F_s \left(\frac{S_o}{N_o} \right)_{min} \quad (2-8)$$

Here, F_s , the system noise figure, includes these other components' noise (temperature) effects in addition to the receiver.

Combining equations (2-8) and (2-6) we have

$$k T_o B_n F_s \left(\frac{S_o}{N_o} \right)_{min} = \frac{P_t G^2 \lambda^2 \sigma_{min}}{(4\pi)^3 R^4} \quad (2-9)$$

Isolating the signal-to-noise ratio gives

$$\left(\frac{S_o}{N_o} \right)_{min} = \frac{P_t G^2 \lambda^2 \sigma_{min}}{(4\pi)^3 k T_o B_n F_s R^4} \quad (2-10)$$

Relaxing the minimum detectable signal values for a moment leaves equation

(2-10) in a form of the radar equation quite suitable for a systems performance analysis. Peebles (5:465) calls a similar equation a system sensitivity equation.

$$\left(\frac{S}{N}\right)_O = \frac{P_t G^2 \lambda^2 \sigma}{(4\pi)^3 k T_O B_n F_s R^4} \quad (2-11)$$

This will be the equation that will be used to compare the CW-nulling and pulse-gated RCS measurement systems in Chapter III. Of the various parameters in equation (2-11), the one that will be of most interest will be the noise figure, F_s .

The system noise figure is derived from physical arguments regarding the effective noise "temperature" of an entire receiving system. To begin, consider the effective noise temperature of the receiver which is related to the noise figure, F_s , as

$$T_e = (F_n - 1)T_O \quad (2-12)$$

where T_e is the effective noise temperature of the receiver. By convention, antennas are treated separately. A parameter called the system noise temperature is defined to account for the effects of an antenna coupling external noise into the receiver. It is defined as

$$T_s = T_a + T_e = T_a + (F_n - 1)T_O \quad (2-13)$$

where T_s is the system noise temperature and T_a is the antenna noise temperature. Finally, the system noise figure is defined as

$$F_s = \frac{T_s}{T_O} = \frac{T_a + T_e}{T_O} = \frac{T_a}{T_O} + (F_n - 1) \quad (2-14)$$

which shows how F_s is related to F_n .

Realistically, a receiver cannot be connected directly to the terminals of an antenna and must, at least, have some intervening transmission line cables or waveguide. In most cases there are even other components that lie in the signal path between the antenna and receiver. To account for the effect on the noise figure of these additional components the noise figure, F_n , in equation (2-14) is replaced with the effective noise figure of cascaded networks, F_o . Skolnik shows F_o to be

$$F_o = F_1 + \frac{F_2 - 1}{G_1} + \frac{F_3 - 1}{G_1 G_2} + \dots + \frac{F_N - 1}{G_1 G_2 \dots G_{N-1}} \quad (2-15)$$

where F_1 and G_1 are the noise figure and gain of the first component encountered in the signal path (from antenna to receiver) and so on (9:345). Thus, equation (2-14) becomes

$$F_s = \frac{T_a}{T_o} + (F_o - 1) \quad (2-16)$$

and this will be the equation used to calculate system noise figure's in the next chapter.

Equation (2-11) can be modified to include losses in the transmit circuitry by adding a loss term, L_t to the denominator of equation (2-11)

$$\left(\frac{S}{N}\right)_o = \frac{P_t G^2 \lambda^2 \sigma}{(4\pi)^3 k T_o B_n F_s L_t R^4} \quad (2-17)$$

Note that this loss term is only for components in the transmit circuit and one should avoid the temptation to include receive circuit loss values in this term. Receive circuit losses have already been accounted for in the system noise figure, F_s .

In the following chapter, equations (2-11) and (2-17) will be used to compare the CW-nulling and pulse-gating RCS measurement systems. More specifically, the factors F_s and L_t in the equations will be compared since actually plugging values into these equations gives misleading results. It will be shown that P_t for the pulse-gating system is far less than P_t for CW-nulling due to the pulse modulation effects. It is entirely possible to recover this loss of power merely by raising the RF source power output. As noted by Mentzer, this can result in improved S/N characteristics for the pulse-gating system but not for the CW-nulling system (1:123). This is because neither of equations (2-11) or (2-15) account for the multitude of clutter sources which exist within the anechoic chamber. Therefore the chamber can only be idealized in these equations and only the loss due to target range (R^{-4}) is included in them. The effects on the two systems of the chamber clutter sources is taken up in Chapter IV.

III Systems Performance Analysis

In this chapter the CW-nulling and pulse-gated RCS measurement systems will be compared on the basis of signal-to-noise ratio (S/N) and sensitivity calculations. Initially, these calculations will be based on idealized models and will then be modified to account for more realistic models including component losses and noise figures. Note that in this chapter no consideration will be given to the anechoic chamber transmission medium. Although it is certainly true that the transmission medium is a necessary part of the overall communication system for analysis purposes, analysis of the chamber and the resultant background characteristics will be postponed until the next chapter. The transmission medium is thus idealized. It is felt that by first looking only at the hardware components of the two systems, an idea of the relative complexities and S/N characteristics can be obtained.

A block diagram of a generalized instrumentation radar system and far-field anechoic chamber arrangement is shown in figure 3.1. In the large component block would be located either the CW-nulling loop or the pulse-gating units and the pulse-gating control equipment.

The system components common to both systems and a short synopsis of RCS measurement procedures are described as follows. The RF source is a Watkins-Johnson (WJ) 1250A microwave synthesizer. The receiver is a Scientific-Atlanta (SA) 1750 phase-amplitude receiver. The azimuth angles of the target positioner are fed to an SA digital position display. For fixed frequency measurements the data is collected as the target continuously rotates. When data has been collected over all aspect angles

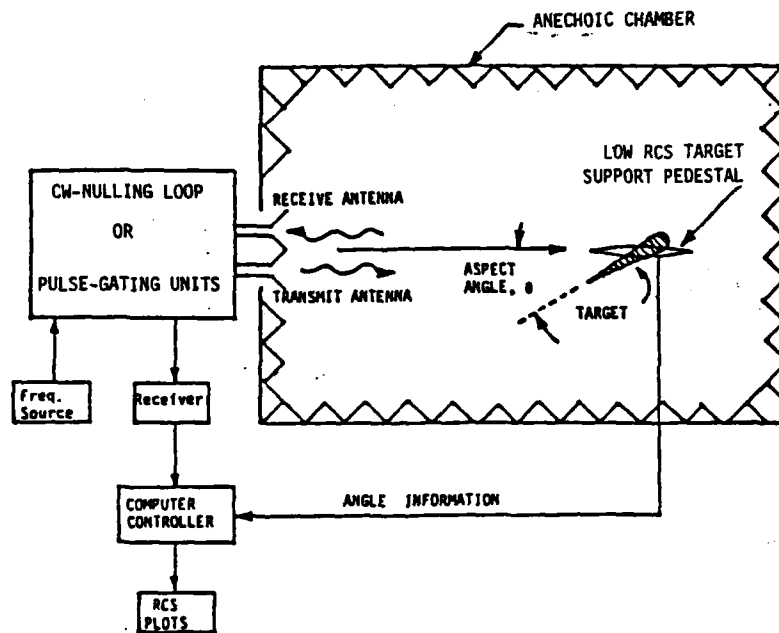


Figure 3.1 Simplified Diagram of a Far-Field Chamber With Generic RCS Measurement System

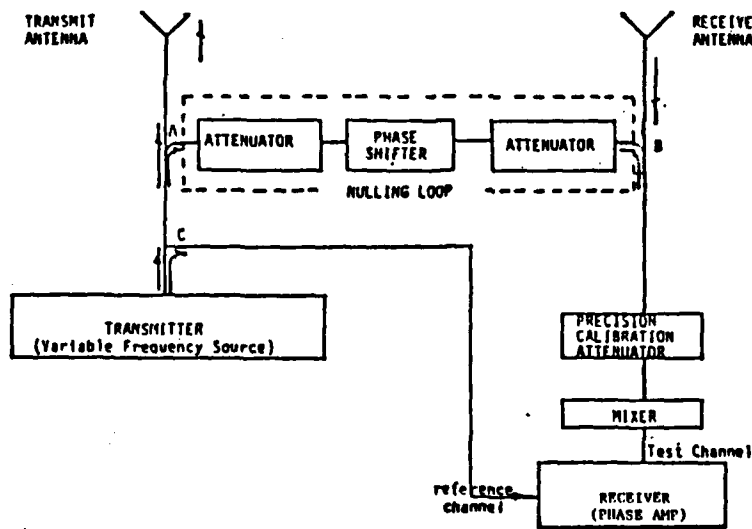


Figure 3.2 Simplified Diagram of CW-Nulling System

of interest the target is turned to the point of highest RCS. The data is then "linearized" by adjusting a precision attenuator through 5 dB steps of increasing attenuation. Normally this linearization takes place over a 60 dB range, equivalent to the dynamic range of the SA 1750 receiver. Once the target RCS data has been linearized a calibration target of known cross section (an 8 inch sphere of -14.9 dBsm cross section) is placed in the chamber and measured. This adjusts the linearized levels of target RCS data relative to the known calibration target. Once these calibration steps are complete the system yields calibrated RCS data versus azimuth angle of the target.

A. Idealized CW-Nulling System

The CW-nulling system utilizes the "nulling loop" of figure 3.2. At point 'A' a portion of the transmit signal is diverted through two precision waveguide attenuators and a precision waveguide phase shifter. In the absence of a target, the only signal entering the receive antenna is that due to clutter sources in the chamber. At point B this "background signal" is combined with the signal from the nulling loop. The nulling loop phase shifter and attenuators are then adjusted so that the signal is equal in amplitude but opposite in phase to the background signal, hence cancelling the background signal in the remainder of the receive circuitry. In this manner the signal level in the receiver is reduced to the lowest possible level, the noise level of the SA 1750 receiver.

Note also that a small portion of the transmit signal is diverted from the system at point C. This signal is used as the phase reference signal in the receiver. Once the receiver is phase-locked to this signal, highly accurate amplitude and phase measurements can be made on this system.

In the following analysis the system will be considered ideal in that all waveguide and transmission cables are assumed lossless and noiseless. The antennas are assumed to contribute no noise to the system and the nulling loop is assumed to be capable of cancelling any background signal. Thus in the idealized CW-nulling case the entire system noise is dominated by the receiver and its inherent noise figure.

The noise figure of the receiver can be calculated from receiver specifications and equation (2-7), the minimum detectable signal. This was given as

$$S_{\min} = kT_o B_n F_n \left(\frac{S_o}{N_o} \right)_{\min} \quad (3-1)$$

According to manufacturer specifications (10,11) the sensitivity of the SA 1750 is defined for a minimum S/N of 1 or 0 dB. For the specific case of X-band operation the SA 1750 receiver sensitivity is listed as -110 dBm (10), thus

$$-110 \text{ dBm} = 10 \log(kT_o) + 10 \log(B_n) + 10 \log(F_n) \quad (3-2)$$

Since

$$kT_o = \left(1.38 \times 10^{-23} \frac{\text{W}}{\text{Hz} \cdot \text{K}} \right) (290^\circ \text{K}) = 4 \times 10^{-23} \frac{\text{W}}{\text{Hz}}$$

then

$$10 \log(kT_o) = -204 \text{ dBW} = -174 \text{ dBm}$$

This leaves

$$10 \log(B_n) + 10 \log(F_n) = 64 \text{ dB} \quad (3-3)$$

From (11), $B_n \cong 15 \text{ kHz}$ or $10 \log(B_n) \cong 41.8 \text{ dB}$. Substituting this last value into equation (3-3) leaves $10 \log(F_n) = 22.2 \text{ dB}$ as the receiver noise figure. This may seem like a rather large value for this receiver's noise figure but the SA 1750 has several mixing, pre-amplification and filtering stages. Thus the 22.2 dB noise figure covers all these internal functions. Also, for purposes of system comparisons, it is not so critical that this value be absolutely correct, for it will be used whenever the receiver noise figure is needed in future comparison calculations.

The signal power transmitted is linearly related to the amount of signal power received by the RCS measurement system. To get an idea of the signal power transmitted by the CW-nulling system some nominal values for RF source power output will be used. Specifically, the X-band output power is nominally 20 mW. The directional coupler at point C has a value of 16 dB. Hence .5 mW is diverted into the phase reference channel leaving 19.5 mW in the signal channel. The directional coupler at A is a 3 dB coupler so 9.75 mW is diverted through the nulling loop and 9.75 mW to the antenna for target illumination.

If a spectrum analyzer is placed in the circuit at points A and C, all that would be seen would be the single frequency CW signal weighted by the coupling at each directional coupler. At point B the single spectral line would be weighted by the RCS of the target and loss due to the target range. In other words, all signal power is contained in the transmitted carrier frequency. This certainly is not a surprising fact for a CW system.

At the receive antenna, the signal reflected from the target will appear. At point B, the signal is combined with the clutter compensating signal from the nulling loop. In the ideal case, this will not affect the signal reflected from the target. So the receiver sees the 9.75 mW transmitted signal weighted by the RCS of the target and loss due to the target range.

Quickly summarizing what has been discussed to this point in the analysis, the CW-nulling system in the ideal case has a receiver noise figure of 22.2 dB. For such a large receiver noise figure the system noise figure will be relatively unchanged and is taken to be 22.2 dB from equation (2-14) (since the antennas contribute no noise in the ideal case, $T_a = 0$). The signal-to-noise equation becomes

$$\left(\frac{S}{N}\right)_o = \frac{P_t G^2 \lambda^2 \sigma}{(4\pi)^3 k T_o B_n F_n R^4} \quad (3-4)$$

For the X-band system the average gain of each horn antenna is approximately 21 dB. If we take the operating frequency as 9.5 GHz ($\lambda = .0316$ m), then at a range of 45 feet ($R = 13.72$ m) the signal-to-noise equation becomes

$$\left(\frac{S}{N}\right)_o = \frac{P_t G^2 \lambda^2 \sigma}{(4\pi)^3 k T_o B_n F R^4} = (208.2 \times 10^3) \sigma \quad (3-5)$$

This equation defines a relative value of the sensitivity of the CW-nulling system.

B. Idealized Pulse-Gated System

A block diagram of the idealized pulse-gated RCS measurement system is shown in figure 3.3. In place of the nulling loop of figure 3.2 are the transmit and receive pulse-gating units shown in figure 3.4. All other system components are the same.

The fact that a receiver with an effective first IF bandwidth of 15 kHz is being used to detect low duty cycle pulsed RF signals with 20 to 30 nanosecond (nsec) pulsewidths may cause some readers to question the capability of the pulse-gated system to make RCS measurements. As was mentioned in chapter II, this sort of detection had a theoretical basis (5:314), but to illustrate the process an imaginary spectrum analyzer will be placed at certain points in the block diagram of figure 3.3. Again the operating frequency will be assumed to be 9.5 GHz.

At point 'a' the 16 dB directional coupler diverts .5 mW to the phase reference channel of the receiver. The remaining 19.5 mW are applied to the transmit pulse-gate. The spectrum at point 'a' is shown in figure 3.5a.

As the CW signal is passed through the pulse-gate a transformation occurs in the frequency spectrum. At point 'b' the Fourier series coefficient magnitude spectrum would be visible as shown in figure 3.5b. The initial effect of the gating is to lower the RF power that passes

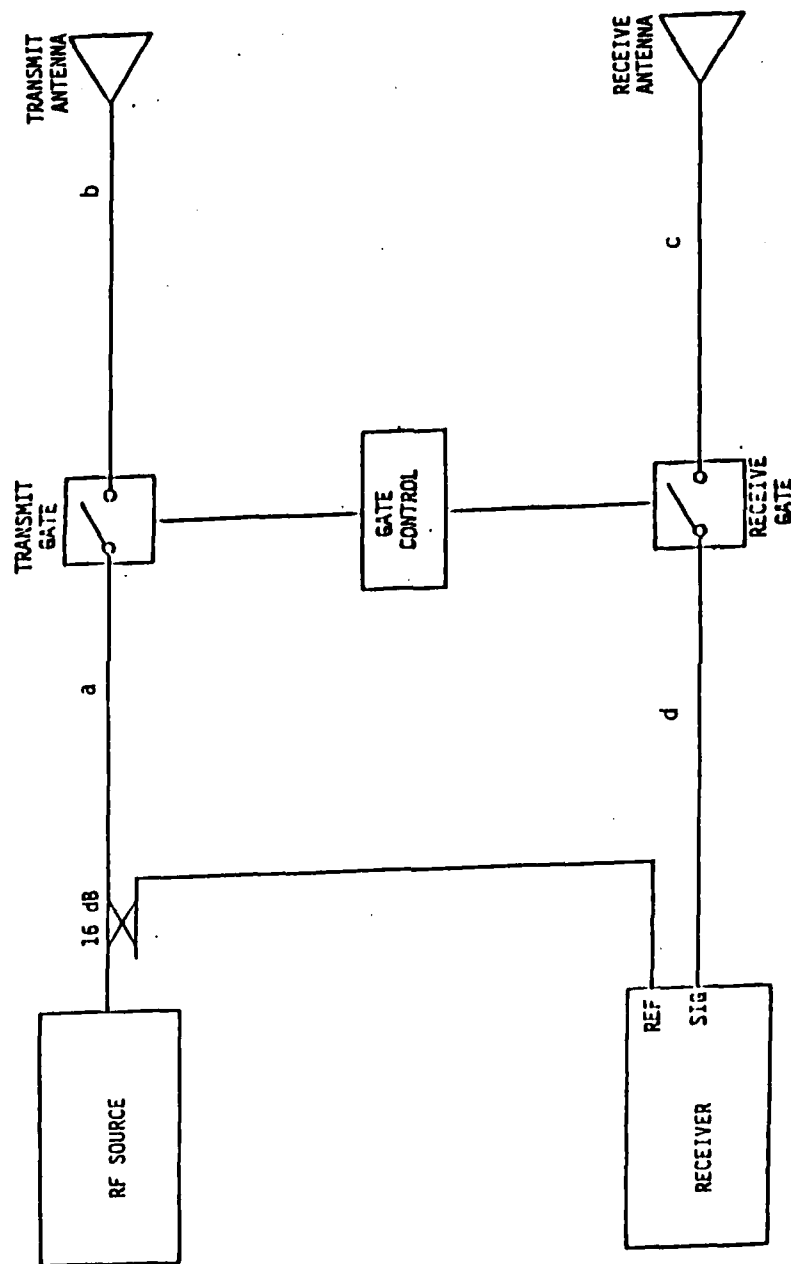
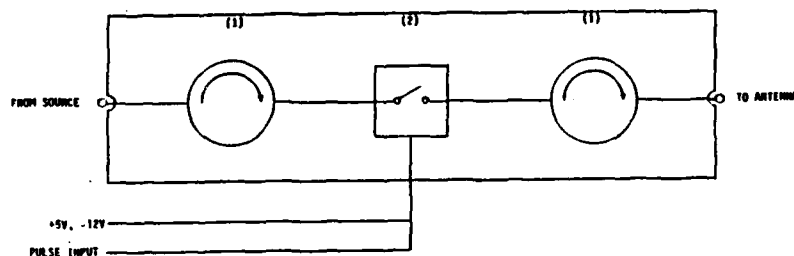
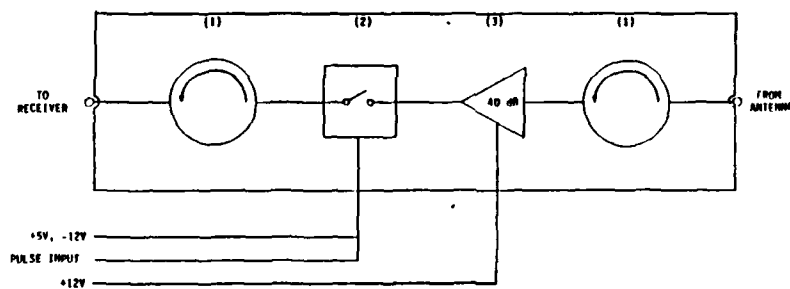


Figure 3.3 Simplified Diagram of Pulse-Gating System



a) Transmit pulse-gating unit



b) Receive pulse-gating unit

- (1) Innowave 6 - 12 GHz Isolators
- (2) General Microwave F192 Nonreflective Switch
- (3) Narda 8 - 18 GHz, 40dB solid state amplifier

Figure 3.4 Block Diagram of Pulse-Gating Units
(Note Low Noise Amplifier in Receive Gate Unit)

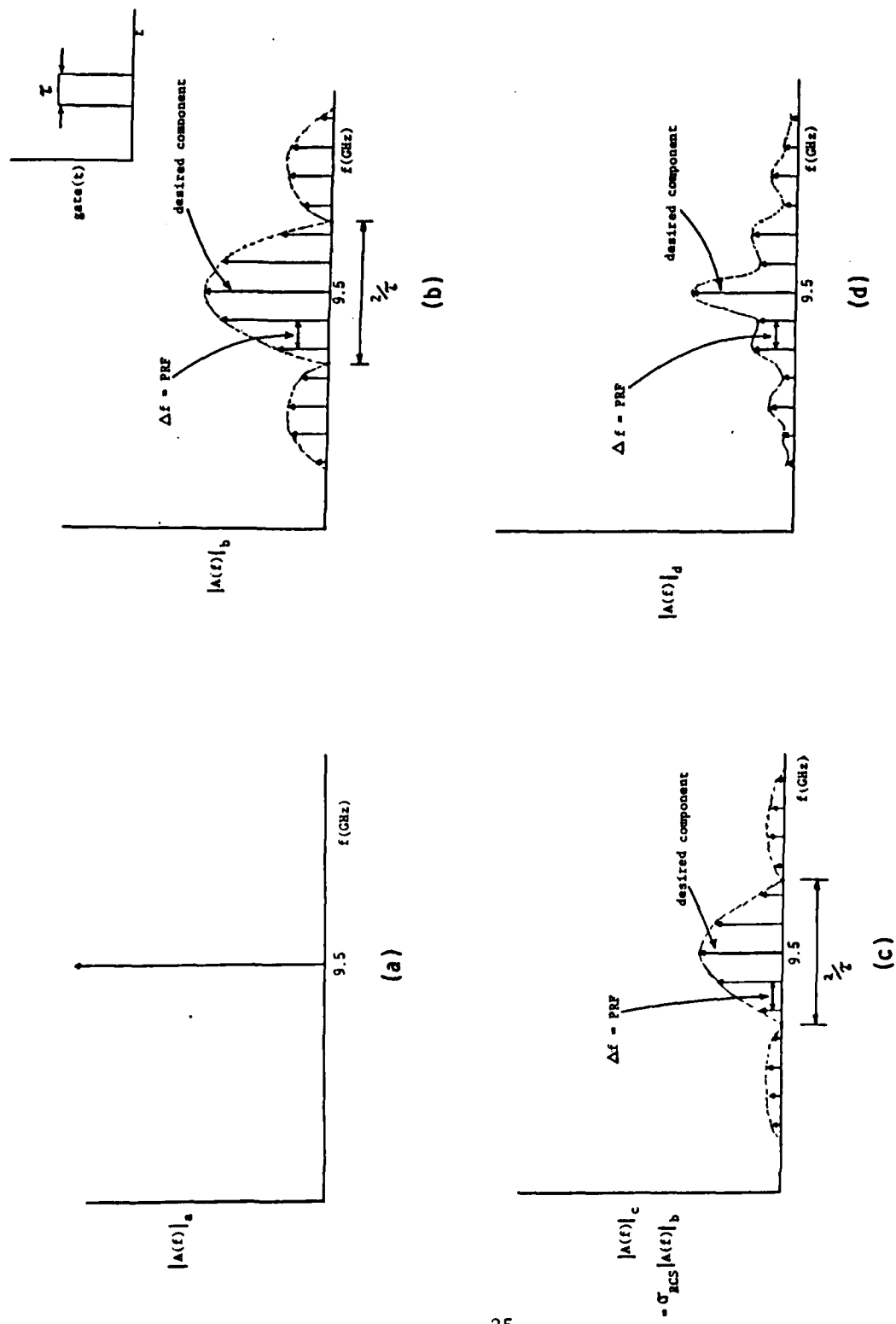


Figure 3.5 Frequency Spectra at Points Highlighted in Figure 3.3 and Figure 3.6

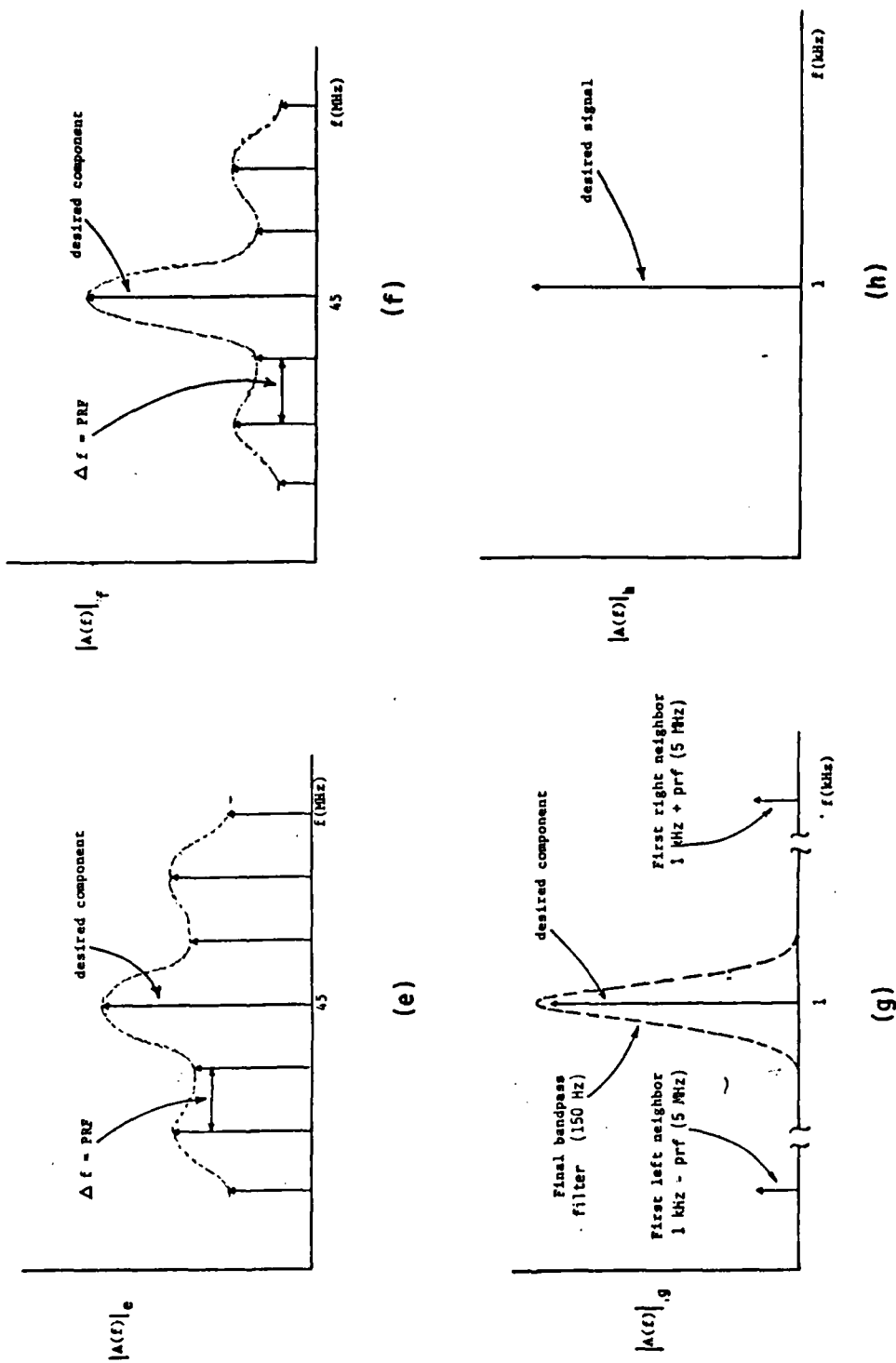


Figure 3.5 continued

through the gates by the duty cycle, τ_t/T . Additionally, the power that passes through the switch is spread over the spectrum of figure 3.5b.

Peebles (5:15) gives the complex Fourier Series representation of a signal as

$$f(t) = \sum_{n=-\infty}^{\infty} C_n \exp\left(j\frac{2\pi n}{T}t\right) \quad (3-6)$$

where $f(t)$ is the time domain representation of the gating signal, C_n is the Fourier series coefficient and T is the period of the gating signal.

C_n is defined as

$$C_n = \frac{1}{T} \int_{-T/2}^{T/2} f(t) \exp\left(-j\frac{2\pi n}{T}t\right) dt \quad (3-7)$$

In the case of an ideal rectangular pulse C_n is just the $(\sin x)/x$ envelope of figure 3.5b in which the spectral lines are separated by $1/T$, the pulse repetition frequency (prf) of the gating signal. For the desired central component of the spectrum, the amplitude of the coefficient is proportional to the duty cycle, τ_t/T

$$|C_0| \sim \tau_t/T \quad (3-8)$$

Where τ_t/T is the duty cycle of the gating signal and τ_t is the pulsewidth of the transmit pulse-gate. The power contained in this component is

(5:22) $|C_0|^2 \sim (\tau_t/T)^2$. Thus the power in the central component is now

$$P_b \sim \left(\tau_t/T\right)^3 P_a \quad (3-9)$$

where P_a is the power at point 'a' in figure 3.3 and P_b is the power at point 'b'. Recalling that P_a was 19.5 mW and using a typical value for τ_t/T of .15 gives $P_b = .066$ mW (proportionality constant taken to be

unity). So in this case P_t , the transmitted power, is .066 mW.

After illuminating the target and returning to the point 'c' in figure 3.3, the spectrum would be the same shape as in figure 3.5b but would be weighted by the RCS of the target and target range attenuation. This spectrum is shown in figure 3.5c, (this is a conceptual sketch, many real targets may distort the envelope by emphasizing or de-emphasizing certain spectral components).

The signal now passes through the receiver pulse-gate to point 'd'. Again, the power in the central component is distributed in a Fourier coefficient spectrum. In general, the receive pulse-gate is narrower than the transmit pulse-gate for reasons outlined by Whitacre (6:56). Since the receive gate "fits inside" the transmit gate, the initial effect would be to lose only an amount of power determined by the ratio of receive gate duty cycle to transmit gate duty cycle or

$$\text{Power loss due to gating} = \frac{\tau_r/T}{\tau_t/T} = \frac{\tau_r}{\tau_t} \quad (3-10)$$

where τ_r is the pulsewidth of the receive pulse-gate. The power in the central component due to spreading is again proportional to (τ_r/T) . Including the signal gain due to the amplifier in the receive pulse-gate unit (figure 3.4) the composite result is

$$P_d \sim 10,000 \left(\frac{\tau_r}{\tau_t} \right) \left(\frac{\tau_r}{T} \right)^2 P_c \quad (3-11)$$

where $P_c = (.066 \text{ mW}) \sigma$. If τ_r/T is taken to be .12, $\tau_r/\tau_t = .8$ and $P_d = (7.6 \text{ mW}) \sigma$ (proportionality constant again taken as unity). This

states that in the pulse-gating case, the power transmitted in the desired spectral component is effectively 7.6 mW. Note that the gain of the solid state amplifier has been included at this point. This gain figure will be taken out later and used to calculate the noise figure of the pulse-gating system. When this is done the effective transmitted power will be reduced by the factor of 10,000 (40 dB) to 760 nW.

The spectrum at point 'd' is shown in figure 3.5d. It is more complicated than $(\sin x)/x$ because of the differences in the pulsewidth's of the two pulse-gates. At this point the signal enters the actual receiver, a simplified block diagram of which is shown in figure 3.6.

The first step in the receiver is a mixing and down conversion of the signal to 45 MHz, the spectrum of which is shown in figure 3.5e. The IF signal is then amplified and filtered to emphasize the 45 MHz component, as shown in the spectrum of figure 3.5f. Note that the desired component at 45 MHz has been emphasized while all other components have been attenuated. This is due to the 15 kHz bandwidth of this first IF filter and the fact that the nearest component is separated from 45 MHz by the prf of the gating signal, typically 3 to 5 MHz. The signal is then mixed and down converted to 1kHz and passed through another frequency selective IF amplifier, which rejects all but the desired signal component. Thus, the final signal is just the central spectral component. One may observe that this signal processing scheme is very closely related to signal recovery by low pass filtering in a pulse amplitude modulation system as described in Peebles (5:314).

We could now return to the illustrative analysis and apply equation (3-4) to the pulse-gating system. The noise figure for this system is

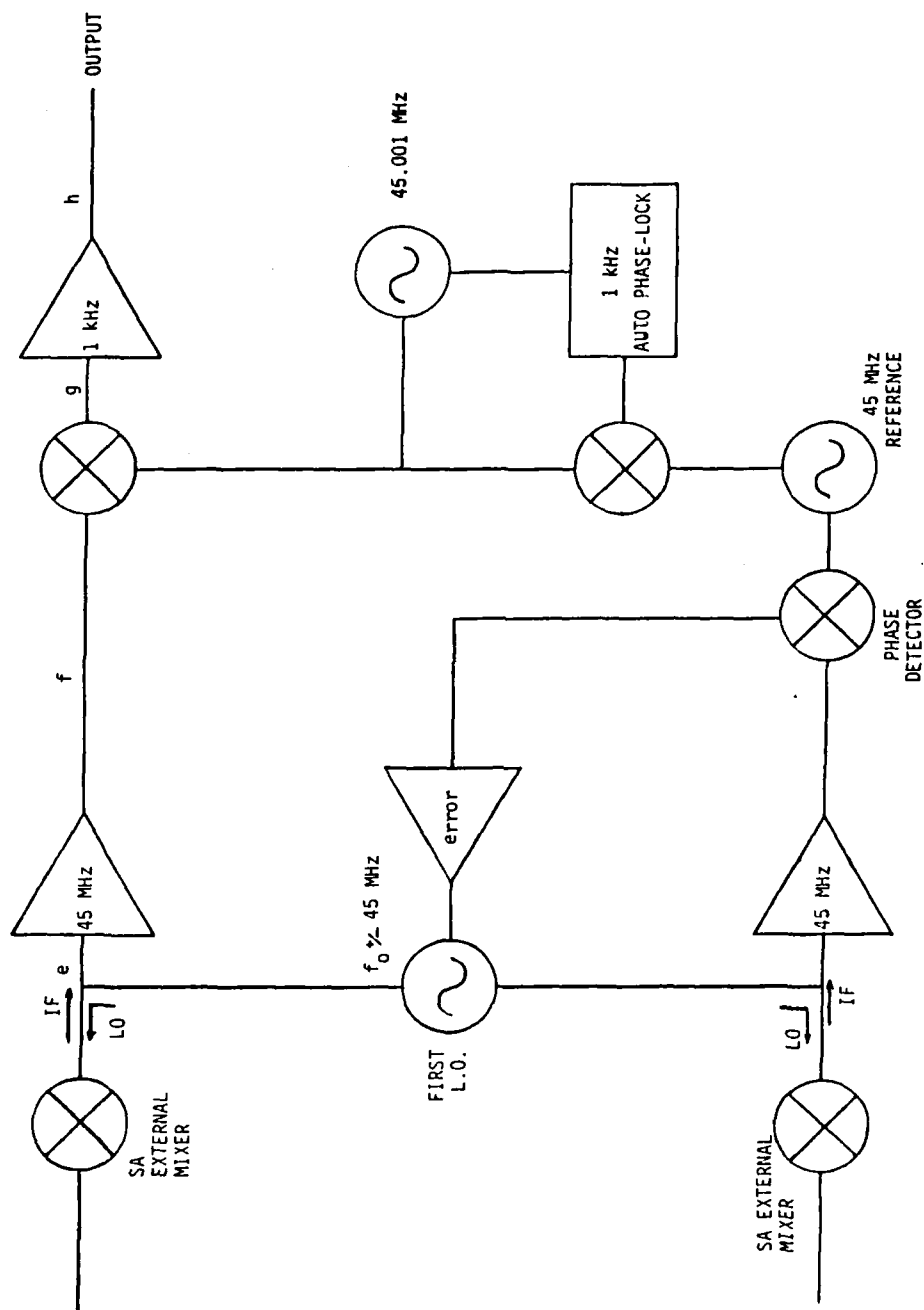


Figure 3.6 Simplified Block Diagram of SA 1750 Receiver

dominated by the low noise amplifier in the front end of the receiving circuitry. Applying equation (2-15) and inserting the values for F_1 , G_1 and F_2 (8 dB = 6.31, 40 dB = 10,000 and 22.2 dB = 165.96 respectively) gives

$$F_o = 6.326 = 8.01 \text{ dB} \quad (3-12)$$

and since in the ideal case, $T_a = 0$,

$$F_s = 5.326 = 7.26 \text{ dB} \quad (3-13)$$

As mentioned earlier, the transmitted power is now 760 nW due to the pulse modulation effects. Carrying through a calculation using equation (3-4) gives the result of

$$\left(\frac{S}{N}\right)_o = \frac{P_t G^2 \lambda^2 \sigma}{(4\pi)^3 k T_o B_n F_s R^4} = (535.3) \sigma \quad (3-14)$$

which is rather misleading in comparison to equation (3-5). Recall that in the pulse-gating system, P_t can be increased without affecting the clutter signal return power. Thus if the RF source power output is increased by some means (using a more powerful source or using a linear amplifier) this value for the pulse-gating system sensitivity can be restored to something more on the order of equation (3-5). The real difference in these systems is in the noise figure, F_s . For the ideal CW-nulling system, $F_s = 22.2$ dB, far more than what is calculated above for the ideal pulse-gating system

Some readers may initially think that this has been a comparison of apples to oranges. It may seem that the results have been stacked against the CW-nulling system by placing a low noise amplifier in the front end of

the receiving end of the pulse-gating system. Obviously, placing this same amplifier in the front end of the CW-nulling system would give the same noise figure result calculated above for the ideal pulse-gating system. However, for the same reason that rendered it impractical to increase P_t in the CW-nulling case to increase S/N, it is not feasible to place an amplifier in the front end of the CW-nulling system and expect to improve the S/N. This is simply because all clutter return signals will be amplified by the same amount as the target return signal, and no real increase in S/N will be obtained. In other words, the sensitivity of the CW-nulling system is "fixed" to a certain value while that of the pulse-gating system is more flexible. This is why looking at just the hardware systems through equations (3-5) or (3-14) is misleading. Upon examination of the time and frequency domain measurements in Chapter IV, the reader will see that in spite of the vast differences in sensitivity predicted through equations (3-5) and (3-14), the pulse-gating system is most certainly capable of out performing the CW-nulling system.

C. Modification of Idealized CW-Nulling System

In Chapter II, equation (2-11) was modified to include loss effects by including a loss term in the denominator. This became equation (2-15). As stated before, the chamber (or transmission medium) is idealized, hence L_t only occurs from transmission line and component losses. The modified equation is repeated here

$$\left(\frac{S}{N}\right)_o = \frac{P_t G^2 \lambda^2 \sigma}{(4 \pi)^3 k T_o B_n F L_t R^4} \quad (3-15)$$

In figure 3.7 the CW-nulling system block diagram is shown with

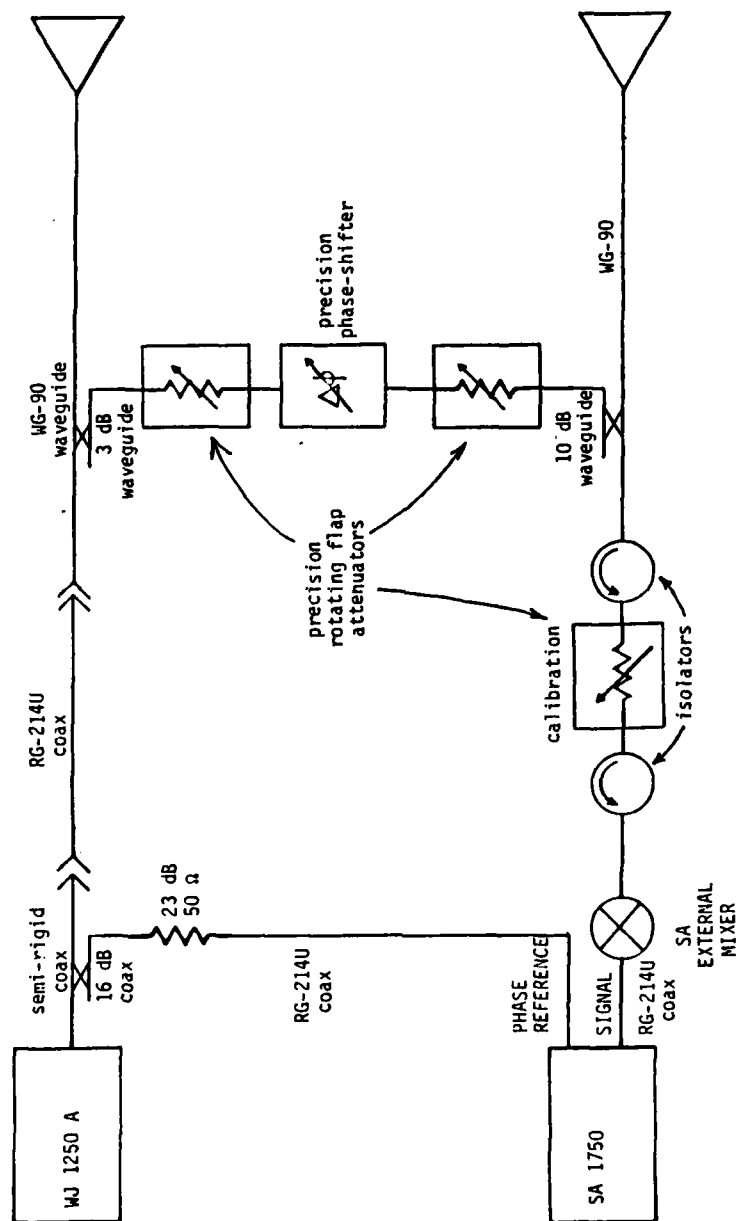


Figure 3.7 Detailed Diagram of CW-Nulling System

specific component types identified. Approximately three feet of semi-rigid coaxial cable leads from the coaxial directional coupler to the RG 214U double shielded coax. Roughly two feet of this cable is then connected to the waveguide adapter. The semi-rigid coax and directional coupler are physically located inside an RF shielded enclosure along with the WJ 1250A. Several adapters are used to convert from one type of coax to the other. With the number of adapters used, the two sections of coax and a 90° bend, the loss in this coaxial section of the system is relatively high. A combination of insertion loss measurements and estimation indicate that a loss of about 4 dB occurs in this section. This is L_c for the CW-nulling system (the directional coupler's 3 dB coupling loss is still assumed ideal and is not included as a loss).

On the receiver side, we will start out with an assumption that the antenna noise temperature is 100°K, just over one-third the ambient level of 290°K. This is a rather low value for antenna noise temperature and is chosen from consideration of antenna noise temperatures for antennas in more normal, outdoor environments (13). It may be that for an indoor anechoic chamber antenna, T_a would be even less than 100°K, but this value is chosen merely for the sake of comparison.

If the WG-90 waveguide is assumed lossless then the first lossy components encountered are the calibration attenuator and its two surrounding isolators. The attenuator has a residual insertion loss of 1 dB when in the normal operating setting (14:40) and each isolator specification plate gives an insertion loss value of 1 dB. The length of RG 214U cable extending from the harmonic mixer to the signal channel input of the SA 1750 is approximately 20 feet. Although this particular

cable was never measured for insertion loss, a value of 3 dB will be assigned to it. Conversion loss in the harmonic mixer is already accounted for in the sensitivity of the receiver in the operating band. Manufacturer specifications show a 5 dB decrease in sensitivity each time the operating frequency doubles from the fundamental (10), (see also Table B.1 in Appendix B of this thesis).

Thus we have $T_a = 100^\circ \text{K}$, $L_t = 4 \text{ dB}$, $F_1 = 6 \text{ dB}$, and $F_2 = 22.2 \text{ dB}$. Applying equation (2-15) to find F_o gives

$$F_o = F_1 + \frac{F_2 - 1}{1/F_1} = 3.98 + 3.98(165.96 - 1) = 660.52 = 28.2 \text{ dB} \quad (3-16)$$

So F_s will be

$$F_s = \frac{T_a}{T_o} + (F_o - 1) = 659.9 = 28.2 \text{ dB} \quad (3-17)$$

Substituting these values for F_s and L_t into equation (3-15) gives

$$\left(\frac{S}{N}\right)_o = (22.08 \times 10^3) \sigma \quad (3-18)$$

Note that L_t is only 4 dB while F_s is increased to 28.2 dB.

D. Modification of Idealized Pulse-Gated System

The modified block diagram of the pulse-gated system is shown in figure 3.8. As in the idealized case the major difference is the replacement of the nulling loop with the transmit and receive pulse-gating units of figure 3.4. Figure 3.8 also shows the pulse-gating control units.

Insertion loss measurements on the transmit pulse-gate box indicate

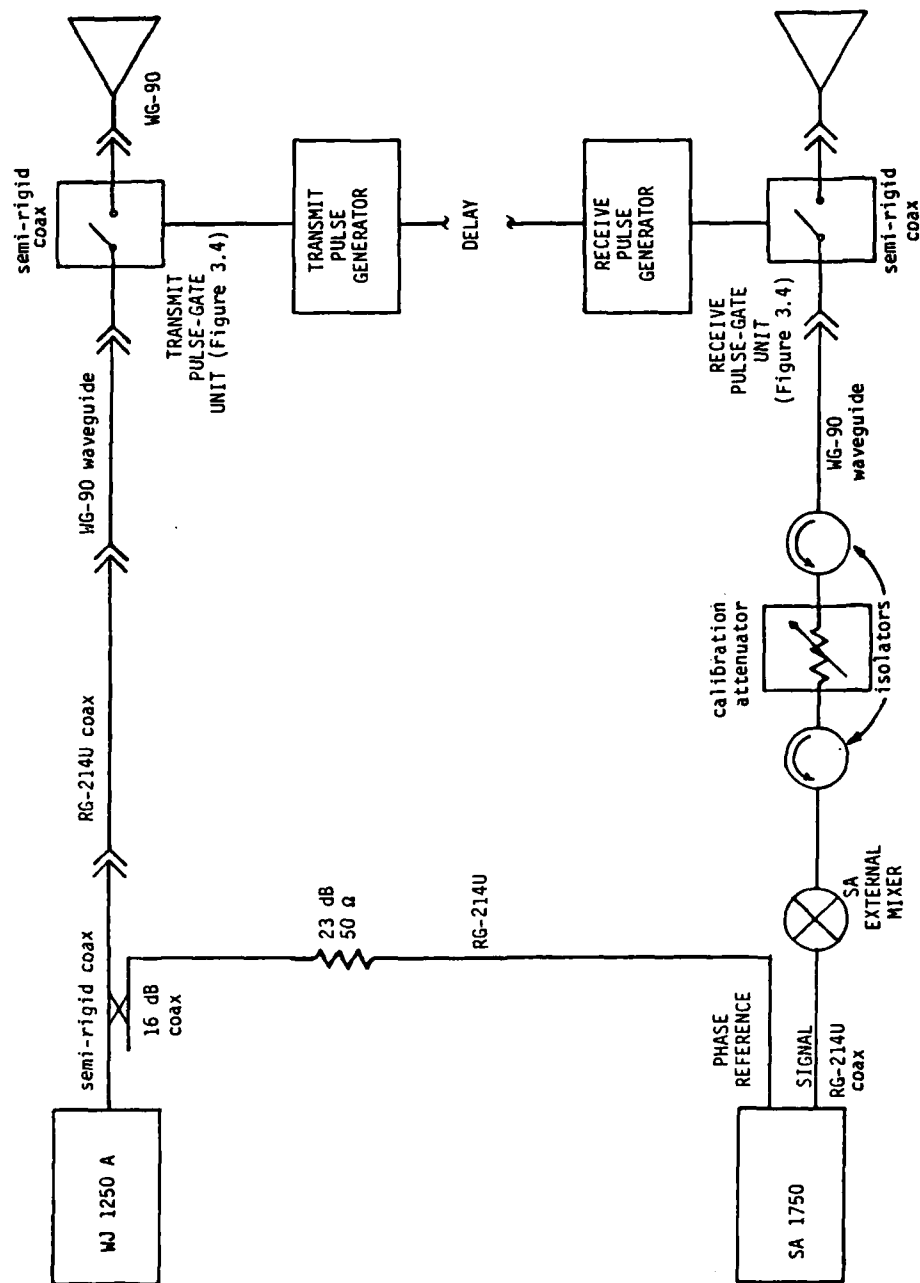


Figure 3.8 Detailed Diagram of Pulse-Gating System

that roughly 5 dB loss occurs when the switches are held open. A fair amount of this could be accounted for by the two isolators, several OSM adapters and chassis mounts and two tight, semi-rigid coax bends needed to fit the components in the RF shielded containers. Although actually measured at 9.37 GHz, a value of 5 dB will be used as the insertion loss at 9.5 GHz. This will include a 1 dB loss for each isolator and 3 dB for the open switch (see Figure 3.4). Thus the transmit pulse-gating unit account for an addition of 5 dB to L_t from the CW-nulling case.

As seen in Figure 3.4, the receive pulse-gate unit contains the low noise, solid state amplifier which provides 40 dB gain to the incoming test signals. Manufacturer specification sheets list a maximum noise figure of 8 dB for this amplifier. Since the amplifier follows the first isolator and precedes the remainder of the circuitry, the switch, the second isolator, calibration attenuator and isolators, and the length of RG 214U cable will be combined into a loss factor of 10 dB. Applying equation (2-15) gives for the cascaded noise figure

$$F_o = 8.16 = 9.12 \text{ dB} \quad (3-19)$$

With $T_a = 100^\circ\text{K}$ assumed, this gives for F_s ,

$$F_s = \frac{100^\circ}{290^\circ} + (8.16 - 1) = 7.5 = 8.75 \text{ dB} \quad (3-20)$$

Thus, for the pulse-gating system, $L_t = 9 \text{ dB}$ and $F_s = 8.75 \text{ dB}$. Comparing results with section C, we see that L_t has increased by 5 dB but F_s has been improved by over 19 dB. This gives a net noise figure/loss improvement of 14.5 dB when operating the pulse-gating system instead of

the CW-nulling system. Note that if the actual values are substituted into equation (3-15) these improvements would be masked by the decrease in transmitted power P_t . However, the arguments given at the end of section B apply to these modified systems as well, so this calculation will not be presented here.

E. Additional Comments and Comparisons

In the preceding sections the CW-nulling and pulse-gated systems were analyzed using sensitivity or S/N equations. Although these equations are well known and widely used, they can never precisely predict an actual system's performance. This is because not every significant loss term in equation (3-15) has been found and included. For instance in the CW-nulling case it was assumed that the directional coupler at point B in figure 3.2 was ideal and presented no additional loss term. It was also rather bold to assume that the nulling loop could compensate or null down to the actual receiver noise level. In this section some of the practical lab experiences will be discussed so that the reader is given a better idea of how these systems compare in actual operation.

The method used to check the depth of a null or the magnitude of the background signal is rather straightforward. In the case of CW-nulling the chamber is first nulled as best possible and that level marked on the chart recorder. Then the 8 inch diameter sphere is mounted and the system response to -14.9 dBsm is noted. The sphere is then removed and the system response is examined for two things: (1) - did the response return to the same level as recorded before mounting the sphere and (2) - how far below the sphere did the system respond? If in the first instance the

answer was no, then the system was re-nulled and the procedure repeated. In the second instance the response was noted and called the background level for that measurement. When the pulse-gated system was operating the procedure was the same except there was no nulling process.

Typical results of this simple procedure during this investigation give us a better idea of how the systems compare in actuality. Not surprisingly, the difference between the achievable background levels for each radar system change on an hourly basis due to the CW-nulling systems null level instability. Typically, the differences between background levels for the two systems are in the 7 to 10 dB range in favor of the CW-nulling system (i.e., -75dBsm CW background to -62 dBsm pulsed background for a difference of 8 dB in favor of CW-nulling). It should be noted however, that the pulse-gating system consistently holds its null level for longer periods of time than does the CW-nulling system. When taking a series of measurements with the CW-nulling system it is necessary to re-null the chamber after each measurement. Obviously this is never the case with pulse-gating since there are no nulling components. This stability factor has a tendency to expedite the measurement process when using the pulse-gating system. Changes in background levels of the pulse-gating system were usually accompanied by a change in weather conditions or vibrations due to building construction. Either of these conditions would make it necessary to abandon further measurements until conditions were back to normal. These stability concerns cannot be modelled by equation (3-15).

Another effect that cannot be taken into account in equation (3-15) is that which electromagnetic interference (EMI) has on a system such as

these. In the case of CW-nulling it is quite easy to compensate for any interfering signal, such as a signal directly coupling from the transmitter to waveguide joints in the receive circuit. It just becomes a part of the background signal that must be cancelled.

The effects of EMI on the pulse-gated system are quite another matter. Since no clutter compensation is used extreme care must be used to keep EMI out of the circuit. This means using metallic tape on every waveguide joint, especially butt-to-butt joints (choke-to-butt joints are far superior EMI-wise since choke joints suppress signals that radiate through the flanges). This metallic tape must fit tightly around the seam between the waveguide sections and sometimes must be supplemented with aluminum foil. Another susceptible component is the external waveguide harmonic mixer where the crystal and tuning mechanism mounting scheme have left these necessary items quite prone to EMI. Generally, most of the circuit must be checked for EMI. It is a time consuming, but absolutely essential step to obtaining a top performing pulse-gating system.

To detect EMI trouble spots, look for the reciprocal effect, the joint or component that leaks or radiates RF. A spectrum analyzer and a small horn antenna are quite effective in locating these components. Sometimes it is necessary to step through the circuit one component at a time, moving a matched termination from one joint to the next, in search of a leaking component. If the reader has the impression that EMI is difficult to find and eliminate, he is correct. It is difficult and time consuming but, again, absolutely necessary because the pulse-gated system can be easily corrupted by stray RF.

Finally, the effect of antenna VSWR and crosstalk in the dual antenna

systems should be mentioned briefly. This problem is especially important in the CW-nulling system since this presents yet another signal to compensate with the nulling loop. The magnitude of this effect is shown in the time domain plots in Chapter IV.

F. S-Band Monostatic System

So far this thesis has considered only CW-nulling and pulse-gating systems operating above 8.2 GHz using a dual antenna system. In this section, a single antenna, monostatic system is considered for operation in S-band frequencies.

The single antenna system uses a magic-tee to isolate transmit and receive arms as shown in figure 3.9. Note that the transmitter and receiver can be interchangeably connected to either arm 1 or 2 of the magic-tee in figure 3.9. Arm 3 is connected to the antenna and arm 4 to the balancing network that nulls the system or compensates for the background signal. The signal from the transmitter divides evenly between arms 3 and 4, and due to background return a signal appears at the receiver from arm 3. The triple stub tuner and other tuning and attenuating devices in arm 4 are then adjusted so that the signal reflected from arm 4 is equal in amplitude but opposite in phase to the background signal from arm 3. Hence this circuit arrangement is capable of cancelling background signals and, ideally, can null down to the receiver noise level.

In the actual system, magic-tee isolation is only about 45 dB between arms 1 and 2. This immediately places a limit on system sensitivity. Also, in an effort to reduce antenna sidelobes, the horn antenna used is

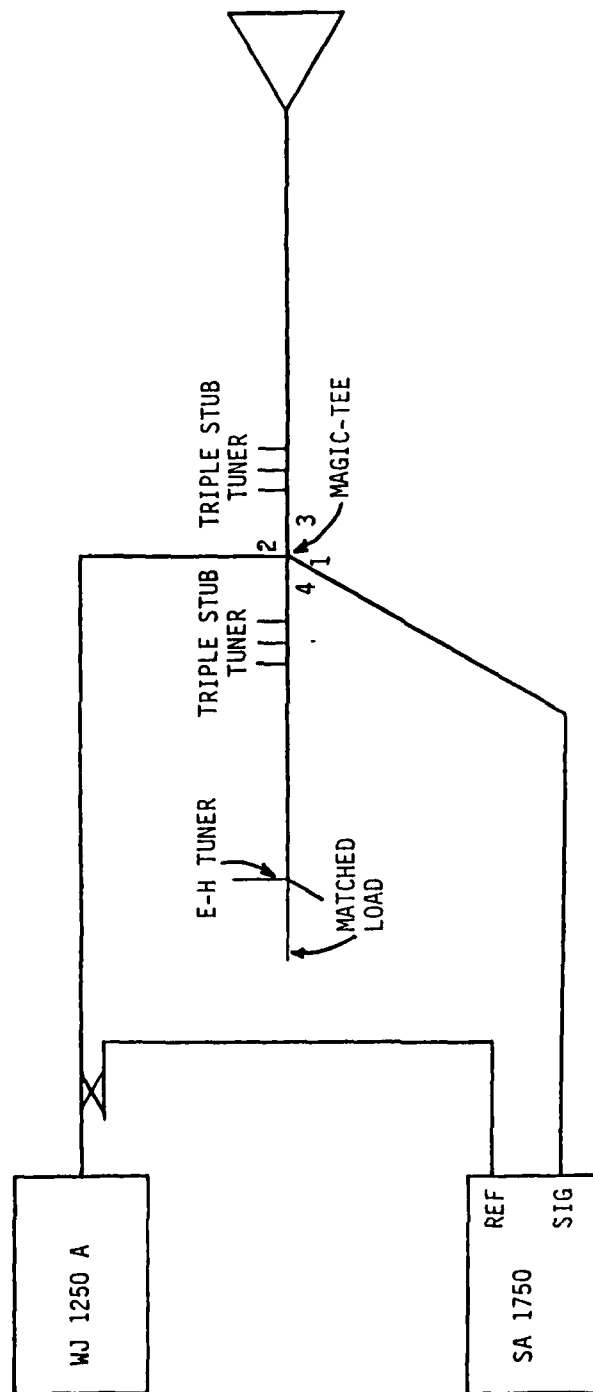


Figure 3.9 Simplified Diagram of S-Band, Single Antenna CW-Nulling System
Using Magic-Tee/Balancing Arm

corrugated for optimum operation at about 3.5 GHz. Operating elsewhere in the band, above or below this optimum frequency, causes antenna VSWR to become a noticeable problem. These two problems have a tendency to degrade the system sensitivity compared to a comparable system employing two antennas and a feedthrough nulling loop.

Eliminating the nulling arm scheme should reduce these effects to some extent. A pulse-gated version of this system is shown in figure 3.10. Ideally the receiver would not "see" any of the ringing due to antenna VSWR or the residual transmitted pulse from the non-ideal magic-tee. Unfortunately, this modified system still did not work. At this point it was decided to abandon the S-band system and return to a dual antenna system. It was not until much later in the investigation that the real source of trouble in the S-band pulse-gating system was identified.

A transient resulting from the DC switching of the gate waveform causes strong spectral components in the 2 to 4 GHz band. This problem is depicted in figure 3.11, which is taken from the actual spectrum analyzer CRT while observing this phenomenon. The desired spectral component and the nearby switching transient component are easily distinguished. This switching transient actually moves through the spectrum, sometimes adding to and distorting the desired spectral component. The effect on the system sensitivity is hard to quantify, but it appears to render the pulse-gated system useless for making low frequency RCS measurements. In figure 3.11, these components are actually observed on a direct signal (as opposed to a reflected RCS signal). The transient is roughly 20 dB below this direct signal, placing a limit on the achievable sensitivity of this system.

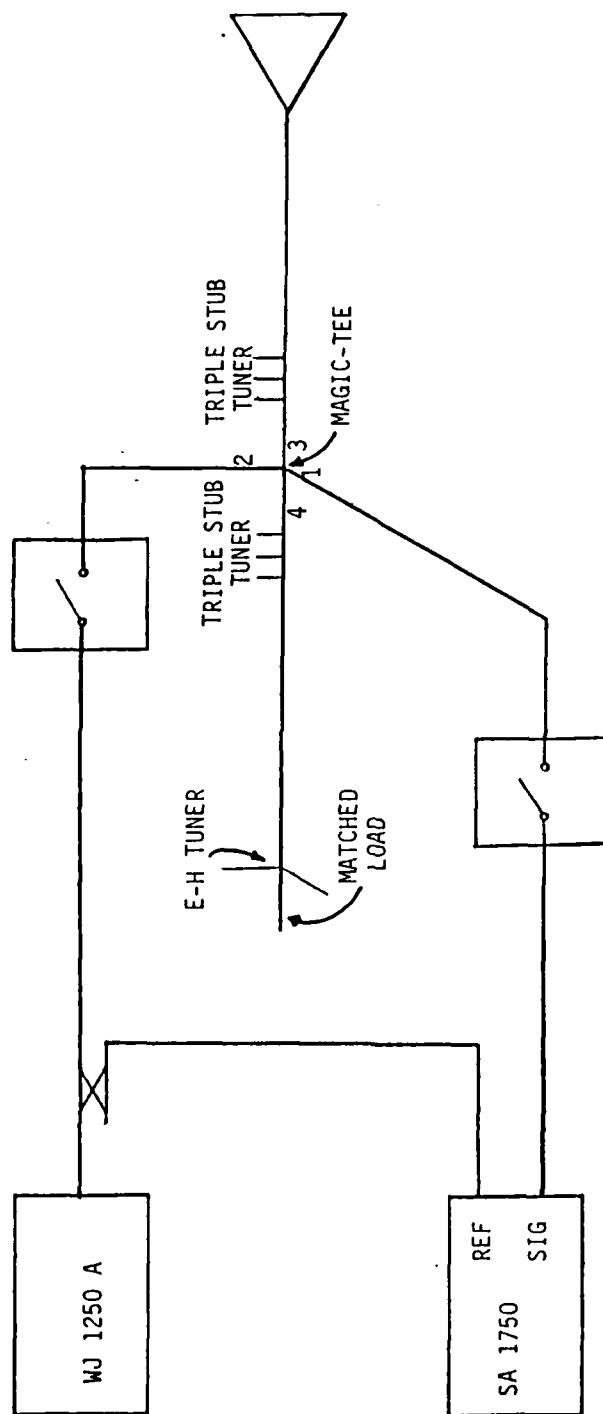
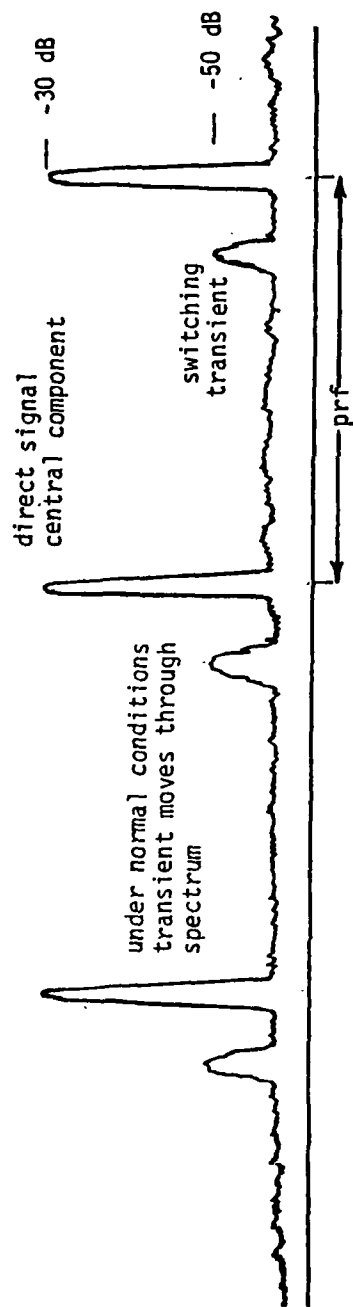
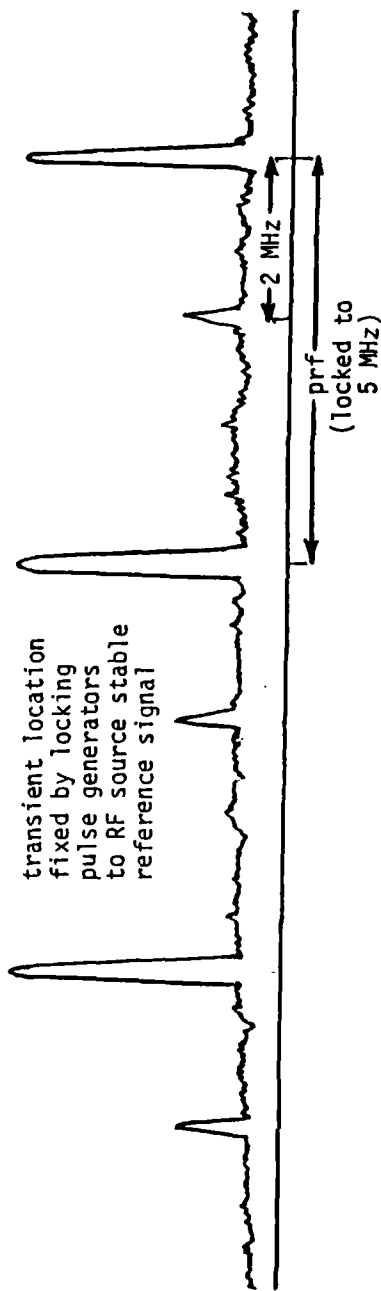


Figure 3.10 Simplified Diagram of S-Band, Single Antenna Pulse-Gating System
(Note the Balancing Arm is Included)



(a) Before Synchronizing To RF Source Reference



(b) After Synchronizing To RF Source Reference

Figure 3.11 Illustrative Spectral Diagram of Switching Transient Relative To Direct RF Signal

Fortunately, the switching transient spectral component can be isolated from the desired low frequency RCS signal. This is accomplished by locking the pulse generators that control the pulse-gates to a steady 5 MHz reference signal available from the WJ 1250A. The RF signal is then offset by 2 MHz from the nearest integral multiple of the desired signal thus restoring system sensitivity. Unfortunately this problem was not identified in time to make RCS measurements for comparison between the pulse-gated and CW-nulling systems on the S-band single antenna system.

IV Comparison of Background Characteristics

In the previous chapter the CW-nulling and pulse-gated systems were compared with no consideration given to any interfering reflections that may occur between the transmit and receive antennas. The assumption was that there were only ideal interactions with the target and attenuation due to target range. In this chapter the effect of chamber clutter sources will be examined. The way in which chamber clutter sources affect the systems' operations and how effectively the system compensates for the clutter signals will be called the system's background characteristics.

To compare the background characteristics of the two systems, moderate resolution time domain diagnostic measurements were performed. These time-domain measurements were made using the pulse-gated system with the RF pulse-gates permanently opened (100% duty cycle). Time domain data is obtained by stepping the RF source and receiver over "N" equally displaced discrete frequencies and inverse Fourier transforming the resulting amplitude and phase data. (The theory behind the time domain system is explained in appendix A.) Since the stepped frequency/time domain measurements are corrupted by any direct feedthrough between the transmit and receive circuits, the nulling loop cannot be employed for these measurements.

A. Time Domain Comparison of Chamber Background Characteristics

The time domain measurements were performed on the 8 inch diameter calibration sphere and a low RCS cone-sphere depicted in figure 4.1. The time domain plot of the far-field chamber with the 8 inch sphere as the

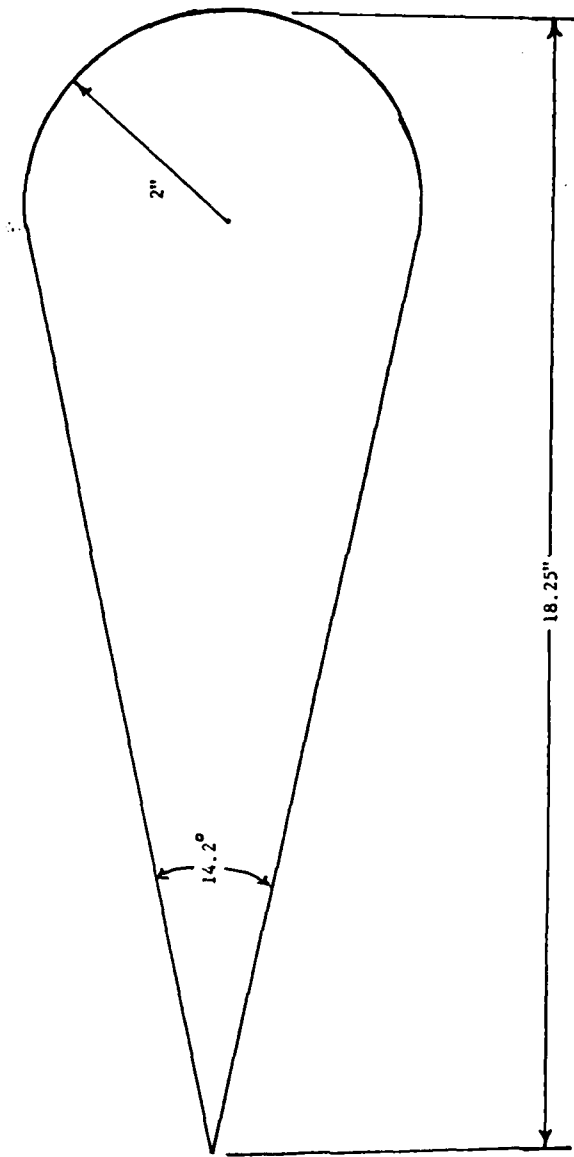


Figure 4.1 Cross-Sectional Diagram of Cone-Sphere Target Shape Used in Time Domain and Fixed Frequency Measurements

target is shown in figure 4.2. As mentioned in Appendix A, this plot represents a time history of the major scattering mechanisms within the chamber. The most significant chamber clutter sources are identified in figure 4.2. The return located at 60 nsec is the direct crosstalk between the transmit and receive antennas, which defines the "front" of the chamber. The chamber length is approximately 65 feet as measured from the antennas to the chamber backwall. The time scale in the time domain measurements is given approximately by,

$$t \approx \frac{2d}{c} \quad (4-1)$$

where t is the time scale, d is the scatterer range (from a reference point, in this case, the front of the chamber) and c is the velocity of propagation. Thus, the scattering from the backwall will occur at approximately,

$$\frac{2(65 \text{ ft})}{1 \text{ ft/nsec}} + 60 \text{ nsec} \approx 190 \text{ nsec} \quad (4-2)$$

The dominant return centered around 135 nsec is the 8 inch sphere. Note that by rearranging equation (4-1) we see that this return corresponds to a distance from the antennas of

$$\left(\frac{(135 - 60)\text{nsec}}{2} \right) 1 \text{ ft/nsec} \approx 37.5 \text{ ft} \quad (4-3)$$

This is the same distance as that of the sphere from the antennas in the chamber. The return spread out in time between 185 - 225 nsec is due to the three-tiered chamber backwall (the second and third tiers are up higher and are farther back from the antennas than the first tier). The clutter return at 165 nsec turns out to be the support pedestal turntable

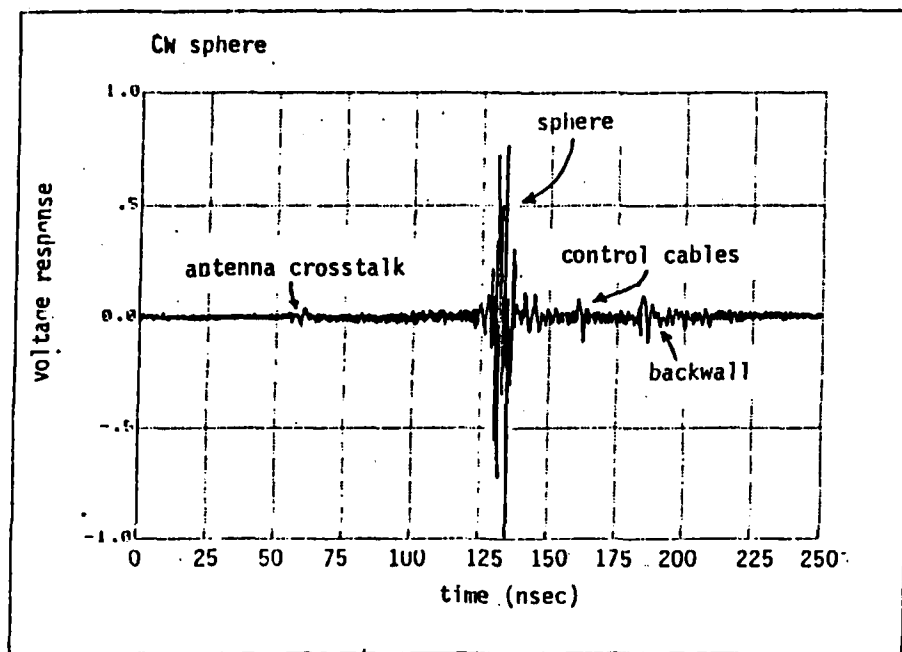


Figure 4.2 CW Time Domain Response: 8 Inch Sphere Mounted on Low RCS Pedestal

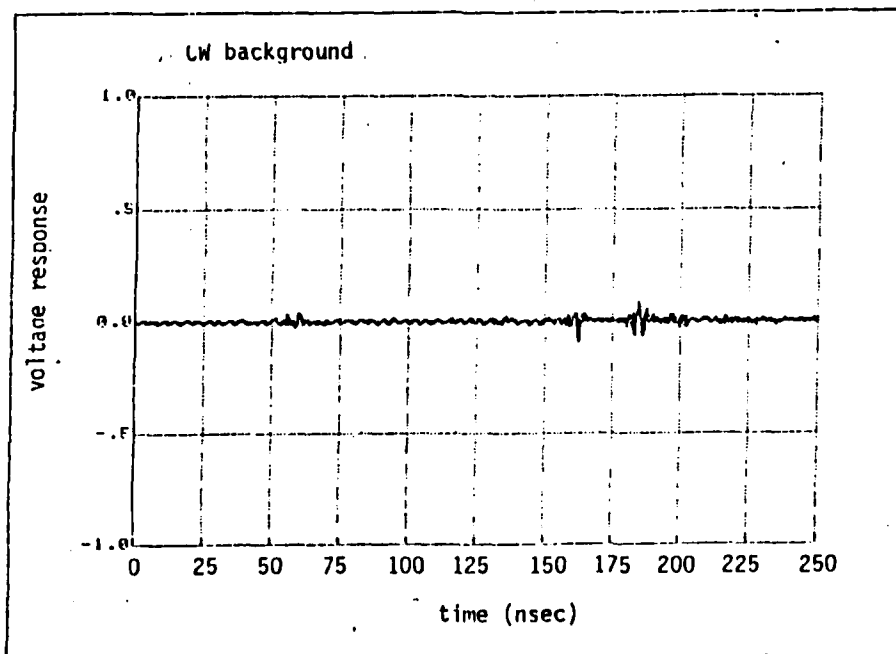


Figure 4.3 CW Time Domain Response: First Background Scan With No Target Present

control cables which are laying on the chamber floor between the chamber sidewall and the support pedestal. This was verified by moving the cables right next to the support pedestal and repeating the time domain measurement. As expected, the cable clutter term at 165 nsec disappeared.

When the sphere was removed and the background measured, the data shown in figure 4.3 was produced. The antenna crosstalk at 60 nsec, the control cables at 165 nsec and the backwall from 185 to 225 nsec are all clearly visible. The target support pedestal is just discernible at 135 nsec. Figure 4.4 is the result of a vector subtraction of the data in figure 4.3 from the data in figure 4.2. All fixed background scatterers have been subtracted out with the exception of the dominant sphere return at 135 nsec. This vector subtraction takes place in the time domain after the data has been inverse Fourier transformed. Using a different computer algorithm, it would be possible to perform this subtraction in the frequency domain before inverse Fourier transforming, (7:1222).

To test the stability of the background measurement, a second background measurement was performed. Figure 4.5 is the result of vectorially subtracting the second background measurement data from the first. Evidently this vector subtraction of the chamber background can reduce the effects of clutter sources within the chamber as supported by the absence of reflections in figure 4.5.

Next, the low RCS cone-sphere of figure 4.1 was placed on the target support pedestal resulting in the time domain plot of figure 4.6. Again the desired target return is centered around 135 nsec. An expanded view of figure 4.6 is shown in figure 4.7. The expansion was taken from 125 to 225 nsec and shows the cone-sphere target at 135nsec, the turntable

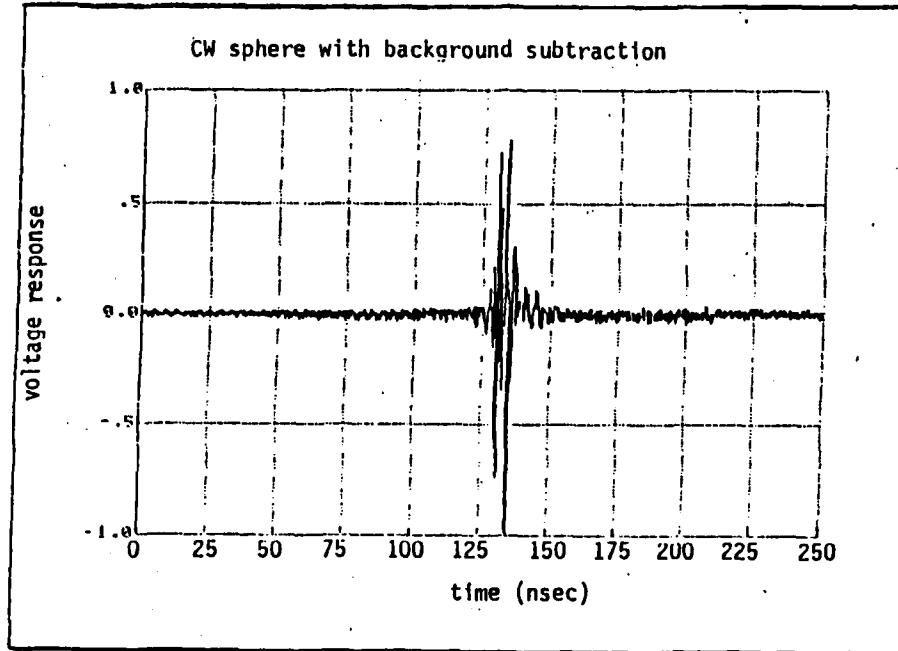


Figure 4.4 CW Time Domain Response: 8 Inch Sphere Minus First Background (subtracting Figure 4.3 from Figure 4.2)

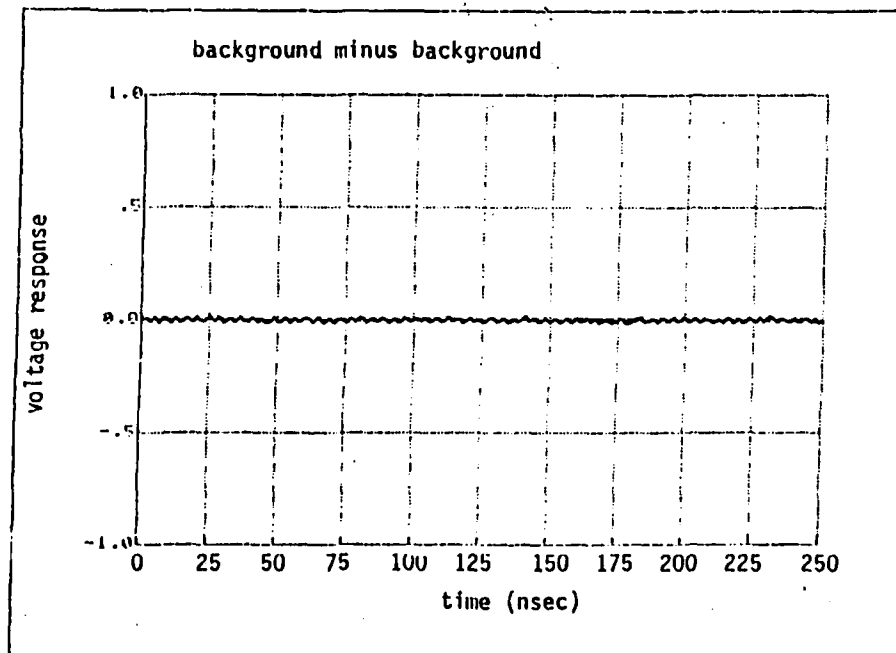


Figure 4.5 CW Time Domain Response: Second Background Minus First Background

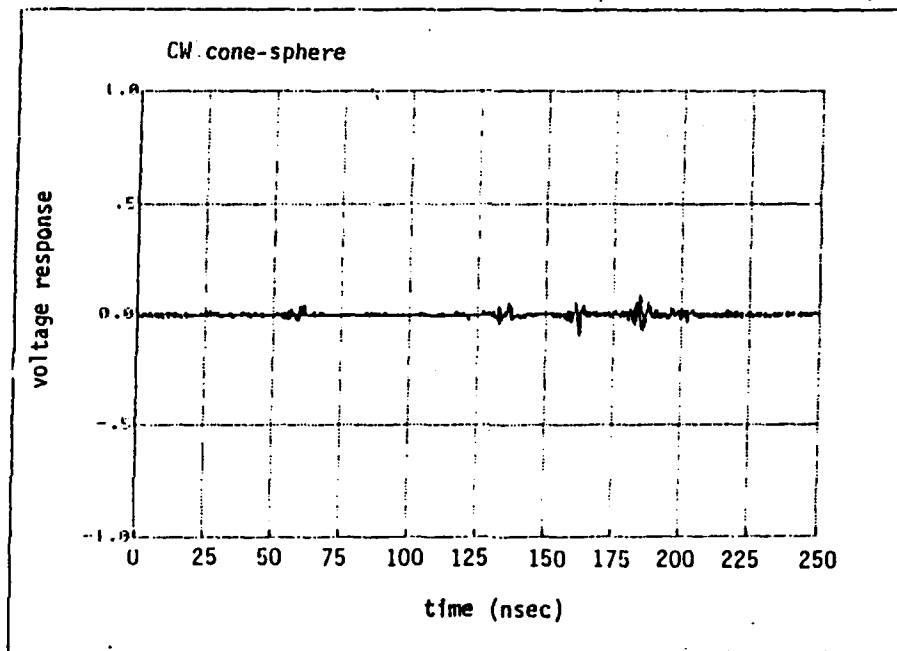


Figure 4.6 CW Time Domain Response: Low RCS Cone-Sphere Mounted on Target Pedestal

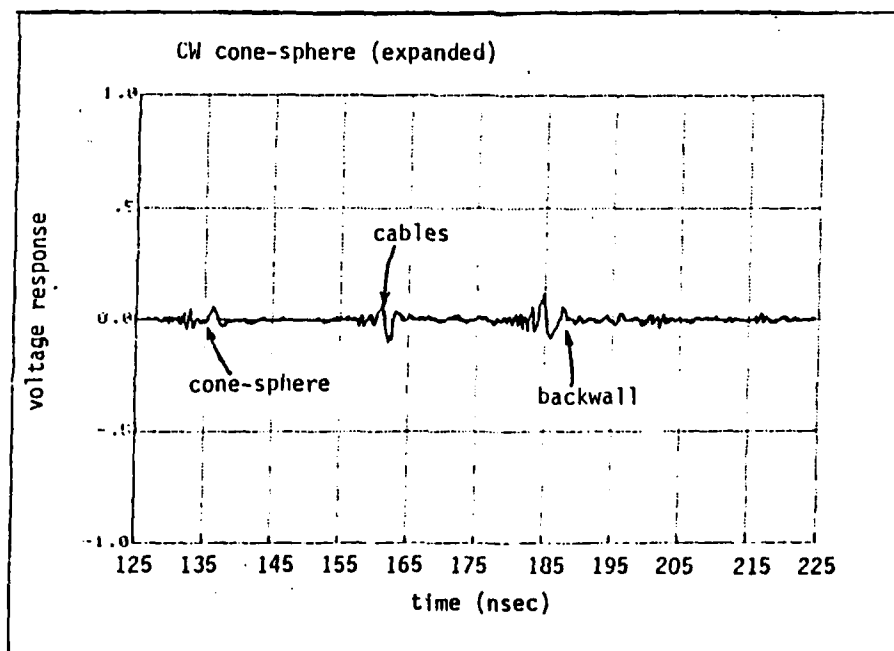


Figure 4.7 CW Time Domain Response: Expanded View of Figure 4.6

control cables at 160 nsec and the chamber backwall from 180 to 205 nsec. Note that the relative amplitudes of these three returns are nearly the same. If the undesired clutter sources are not eliminated it would be difficult for any RCS measurement system to accurately distinguish the cone-sphere RCS from the surrounding clutter RCS. Recall that the CW-nulling system attempts to cancel out the effects of reflections from the clutter sources. When the target RCS is on the same order as the clutter RCS, measured fixed frequency RCS patterns may be seriously in error. This effect will be clearly demonstrated later.

Repeating the vector background subtraction process as with the sphere, the chamber background (figure 4.8) is subtracted from figure 4.6 resulting in figure 4.9. Once again the target can be seen at 135 nsec, easily distinguished from other scatterers in the chamber.

Next, the pulse-gating units were adjusted for pulse-gating operation, (i.e., the duty cycle was adjusted from 100% to about 15%). With the 8 inch sphere mounted on the pedestal the range gate was adjusted so that the target was centered in the range bin. Note that the antenna crosstalk and the chamber backwall returns do not appear in figure 4.10 because they have been completely gated out. Initially, however, the range gate was left too wide, so that the clutter due to the control cables is still visible next to the target sphere return. Note that the return appears to occur at a greater range (longer time) than in previous plots. This is because a modification in the pulse-gating technique was implemented during these measurements. The modification, called fundamental mode mixing, is a technique that increases the overall phase length of the set-up. Longer line lengths translate to longer time delays

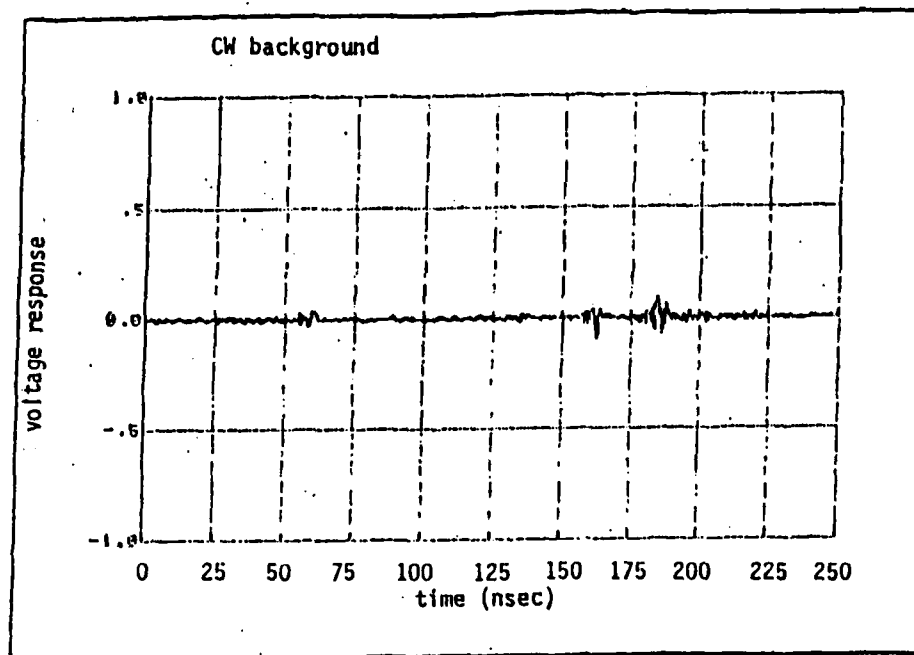


Figure 4.8 CW Time Domain Response: Third Background Scan With No Target Present

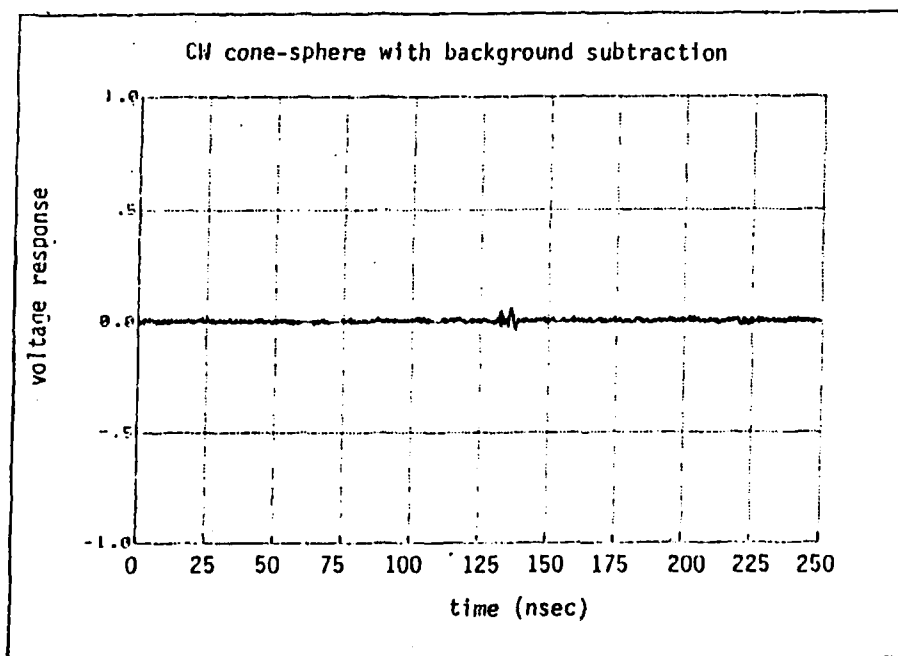


Figure 4.9 CW Time Domain Response: Cone-Sphere Minus Third Background (Figure 4.8)

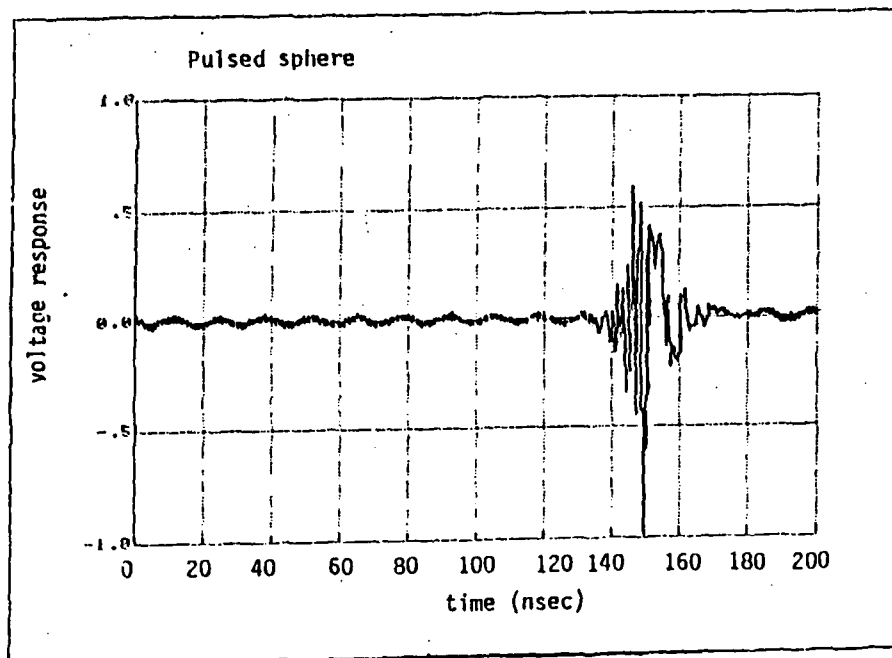


Figure 4.10 Pulse-Gated Time Domain Response: 8 Inch Sphere Mounted on Target Pedestal

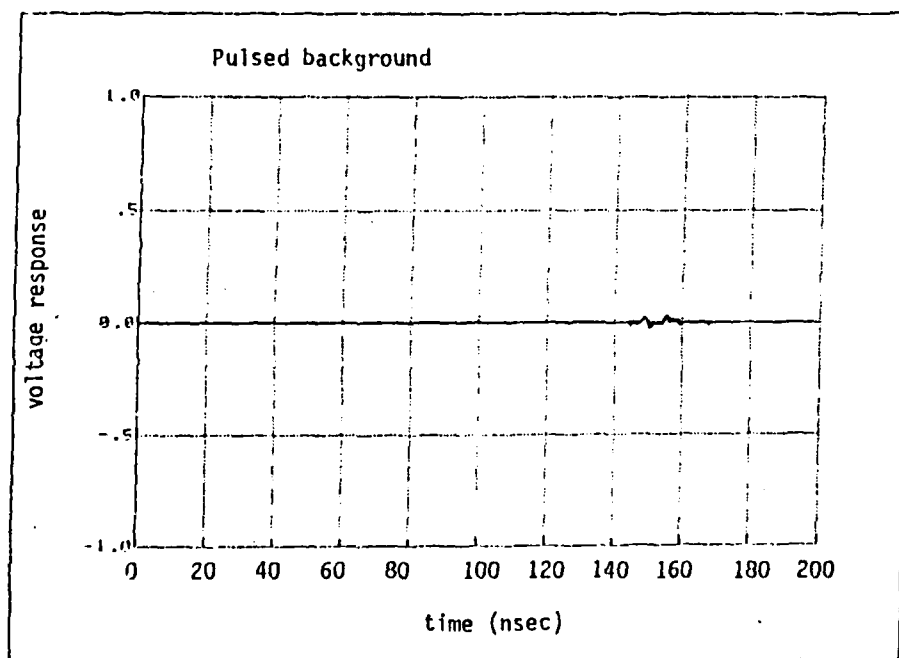


Figure 4.11 Pulse-Gated Time Domain Response: Pulsed Background Scan With No Target Present (Normalized to Sphere Measurement, Figure 4.10)

for the return signal. This technique is described more fully in appendix B of this thesis.

By narrowing the width of the receive gate, the control cables were gated out. Figure 4.11 shows the slight return from the target pedestal when all other clutter sources have been gated out. Note that this plot has been normalized to the same value as in the sphere plot in figure 4.10.

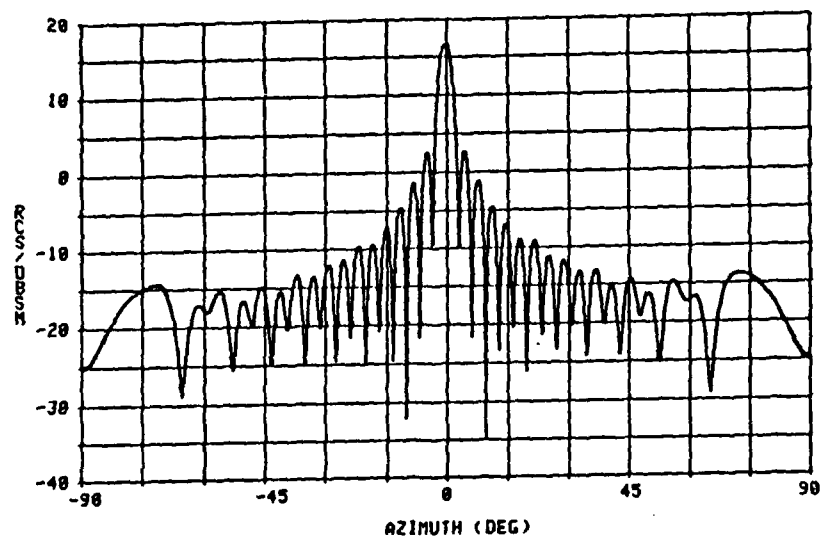
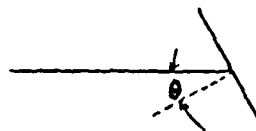
This section has demonstrated that pulse-gating techniques reduce chamber background RCS. The CW time domain plots clearly show that for low RCS targets, the chamber clutter sources can scatter as much energy as the target of interest. It was demonstrated that pulse-gating separates the target area from the spurious chamber clutter sources. Also, it is anticipated that further improvement in overall system sensitivity can be realized by combining pulse-gating with vector background subtraction techniques.

B. Fixed Frequency RCS Pattern Comparisons

Fixed frequency RCS measurements using both the CW-nulling and pulse-gating systems will now be presented for three generic targets. These include a 12 inch square plate, a right circular cylinder 12 inches in length with 3 inch diameter endcaps, and the cone-sphere of figure 4.1. The plate and the cylinder have relatively high RCS characteristics while the cone-sphere has a low RCS in the nose-on region.

Figure 4.12 is the first comparison between CW-nulling and pulse-gated RCS measurements. The top plot is CW-nulling and the bottom plot is pulse-gated. This comparison is for the square plate at 8.5 GHz,

MODEL CW SQUARE PLATE, 7 JUNE 1985
 FREQ 8.5 GHZ POL H RANGE 45



MODEL PULSED SQUARE PLATE, 7 JUNE 1985
 FREQ 8.5 GHZ POL H RANGE 45

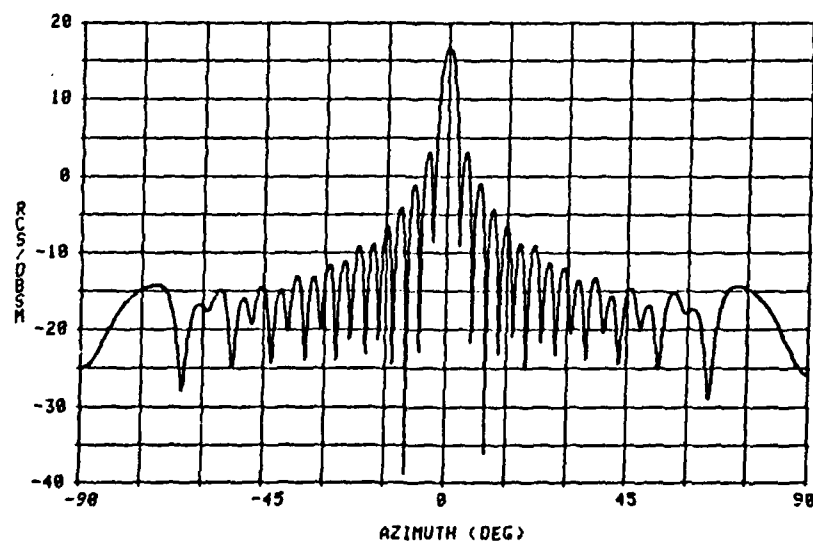


Figure 4.12 CW-Nulling and Pulse-Gating Measurements of a 12 Inch Square Plate
 (8.5 GHz, Horizontal Polarization)

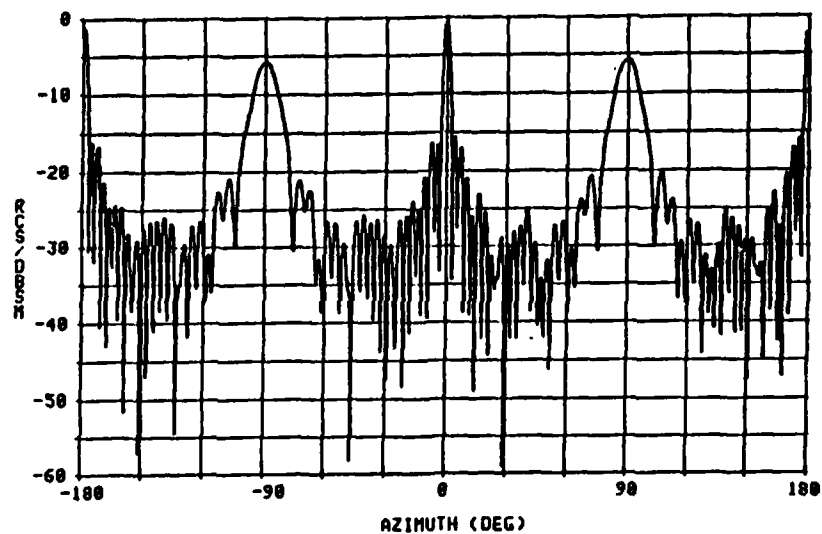
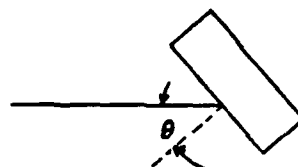
horizontally polarized. If the two plots are aligned very few differences will be noted in the RCS patterns. For this particular target, the two measurement methods yield the same RCS pattern.

The other high RCS target was the cylinder. Figures 4.13 and 4.14 are comparisons of measurements of the cylinder's RCS for different frequencies and polarizations. Figure 4.13 is horizontally polarized at 9.37 GHz (CW-nulling on top, pulse-gated at bottom). Figure 4.14 is vertically polarized at 11.5 GHz. Once again if the CW-nulling and pulse-gated plots are carefully compared, one can find only minor differences in the patterns. Peak levels, sidelobes and the location and depth of nulls line up quite well. Evidently, for high RCS targets, the two techniques perform equally well and give few measurable differences in the resulting patterns.

This equality of performance does not hold, however, when measuring a low RCS target with high forward scattering characteristics. The next series of measurements were made on the cone-sphere target of figure 4.1 at frequencies of 8.5, 9.37, 15 and 18 GHz with various polarizations. Figure 4.15 is horizontally polarized at 8.5 GHz. Notice some subtle differences between the measured patterns. In the nose-on region of low RCS the two techniques appear to see different return characteristics. The main scattering lobe at zero degrees appears smaller and more symmetrical in the pulse-gated pattern. Also the nulls are more clearly defined and deeper in the pulse-gated measurement. The initial interpretation is that the pulse-gated system "sees" a more symmetrical body, and the cone-sphere is a symmetrical body.

Figure 4.16 is a vertically polarized measurement of the cone-sphere

MODEL CW CYLINDER, 5 JUNE 1985
FREQ 9.37 GHZ POL H RANGE 45



MODEL PULSED CYLINDER, 6 JUNE 1985
FREQ 9.37 GHZ POL H RANGE 45

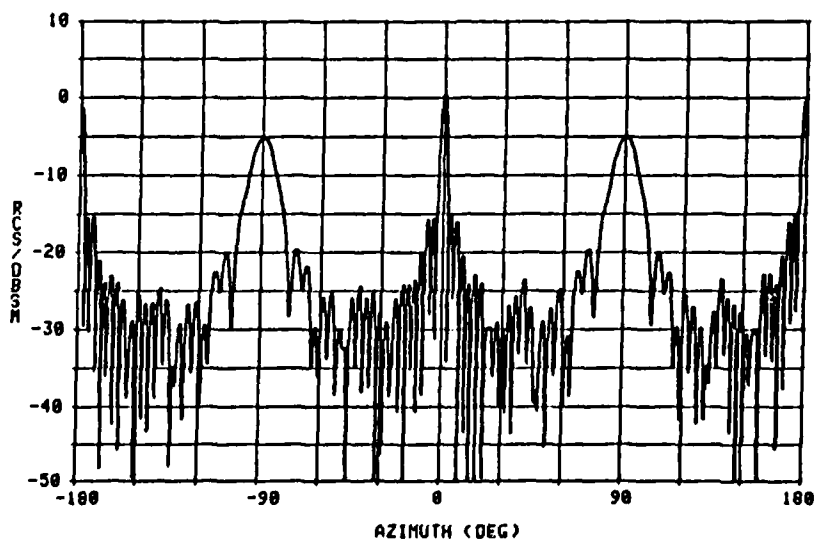
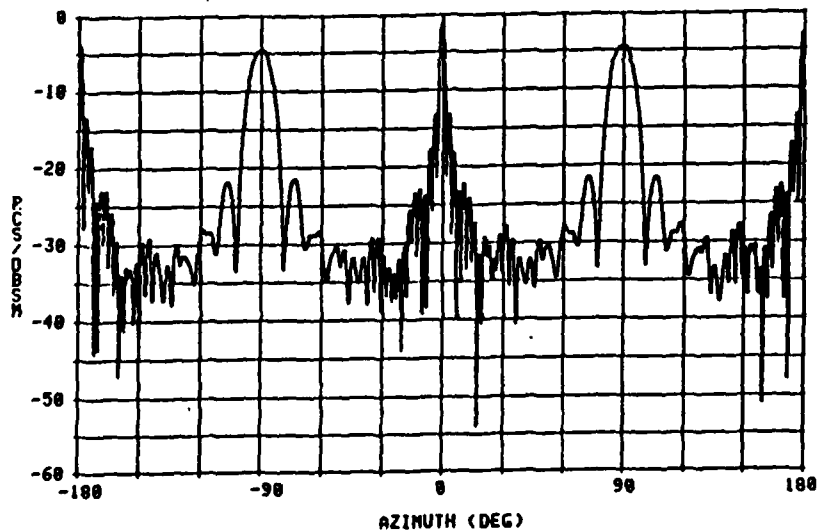


Figure 4.13 CW-Nulling and Pulse-Gating Measurements of a 12 Inch Cylinder (diameter = 3 inches) (9.37 GHz, Horizontal Polarization)

MODEL CW CYLINDER, 5 JUNE 1985
FREQ 11.5 GHZ POL V RANGE 45



MODEL PULSED CYLINDER, 6 JUNE 1985
FREQ 11.5 GHZ POL V RANGE 45

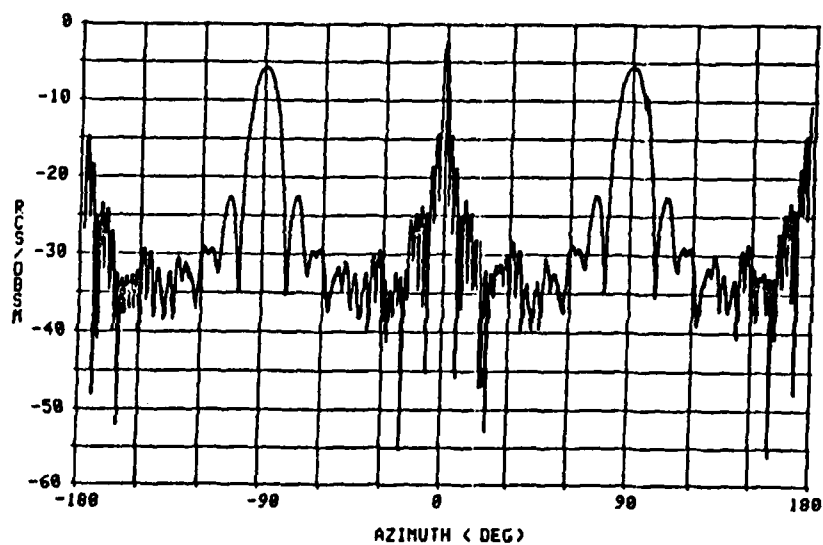
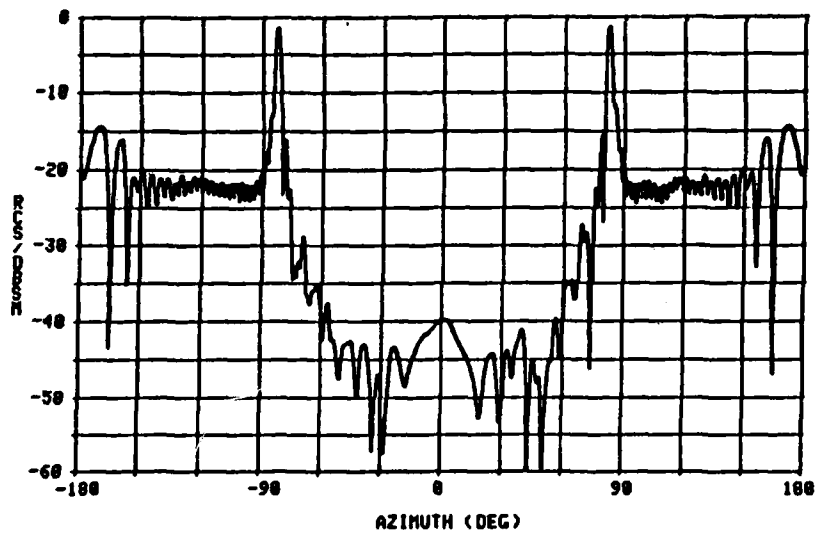
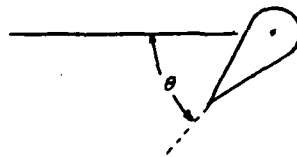


Figure 4.14 CW-Nulling and Pulse-Gating Measurements of a 12 Inch Cylinder (diameter = 3 inches) (11.5 GHz, Vertical Polarization)

MODEL CW CONE-SPHERE, 4 JUNE 1985
FREQ 8.5 GHZ POL H RANGE 45



MODEL PULSED CONE-SPHERE, 4 JUNE 1985
FREQ 8.5 GHZ POL H RANGE 45

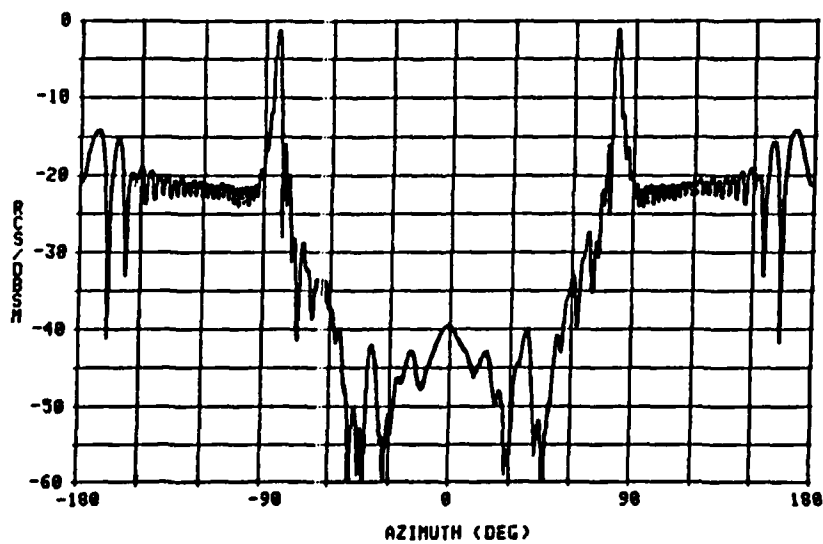
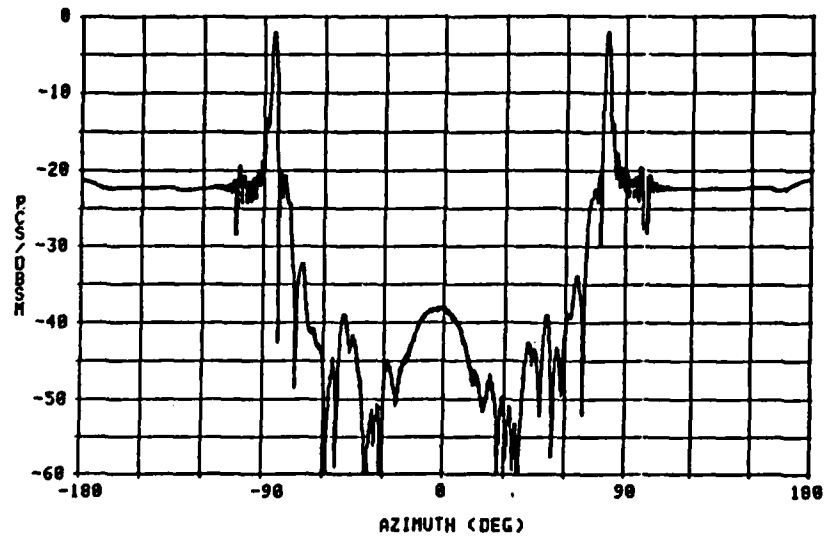


Figure 4.15 CW-Nulling and Pulse-Gating Measurements of a Cone-Sphere
(8.5 GHz, Horizontal Polarization)

MODEL CW CONE-SPHERE, 20 MI. CW CONE-SPHERE, 20 MAY 1985
 FREQ 9.37 GHZ POL U RANGE 45



MODEL PULSED CONE-SPHERE, 21 MAY 1985
 FREQ 9.37 GHZ POL U RANGE 45

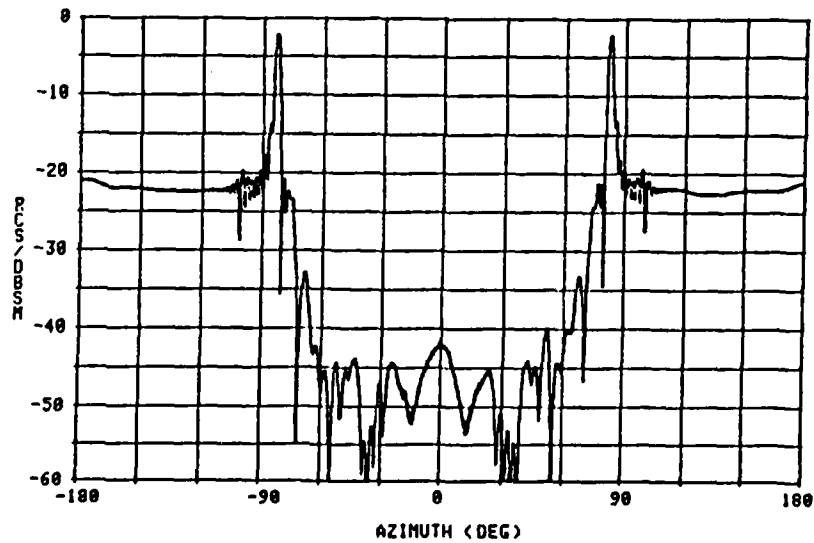


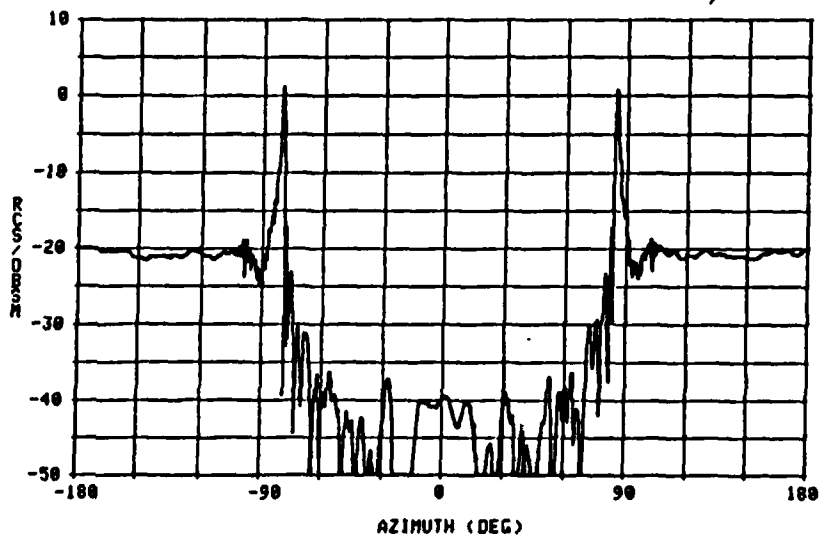
Figure 4.16 CW-Nulling and Pulse-Gating Measurements of a Cone-Sphere
 (9.37 GHz, Vertical Polarization)

at 9.37 GHz. Here we begin to see that the pulse-gated measurement is even more symmetric about the nose-on region of the cone-sphere. This added symmetry may even extend out to the $\pm 40^\circ$ off nose-on aspect. Additionally, the nose-on RCS of the cone-sphere is lower and the main lobe is narrower in the pulse-gated measurement.

Figures 4.17 and 4.18 are vertically polarized measurements at 15 GHz and 18 GHz respectively. In these measurements both systems see deep null levels, many exceeding -50 dBsm. Once again, however, the pulse-gated system unmistakably sees a symmetrical return from the cone-sphere. The CW measurements are nonsymmetric with some severe distortion from $\pm 30^\circ$ from nose-on for both frequencies. An explanation for these stark differences for near nose-on is as follows. When CW-nulling is used, the entire anechoic chamber return is artificially cancelled out by injecting a compensating signal into the receive circuit. Initially then, the chamber backwall is fully illuminated. When a high forward scatter target like the cone-sphere is placed in the chamber, the backwall illumination is altered from the empty chamber condition. These new background field distributions have a different vector sum at the receive antenna than did the old background field distributions, but the compensating signal is still cancelling only the original background signal. If the change in backwall illumination is large enough, the CW-nulling system will be unable to distinguish the target from the background signal. It is believed that this phenomena is responsible for the overall higher levels of measured RCS for the CW-nulling measurements of the proceeding figures.

To test the hypothesis outlined above, a small corner reflector was placed into the backwall absorber. The chamber, including the corner

MODEL CW CONE-SPHERE, 15 APRIL 1985
FREQ 15 GHZ POL V RANGE 45



MODEL PULSED CONE-SPHERE, 11 APRIL 85
FREQ 15.8 GHZ POL V RANGE 45

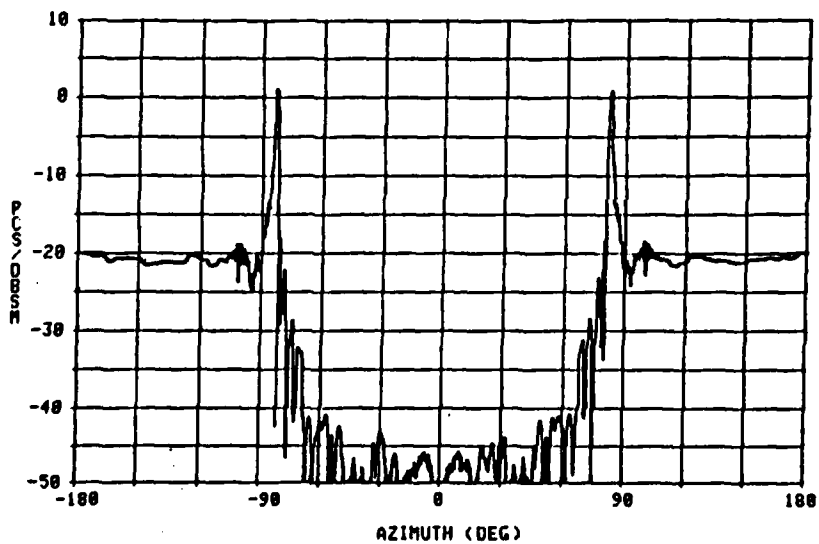
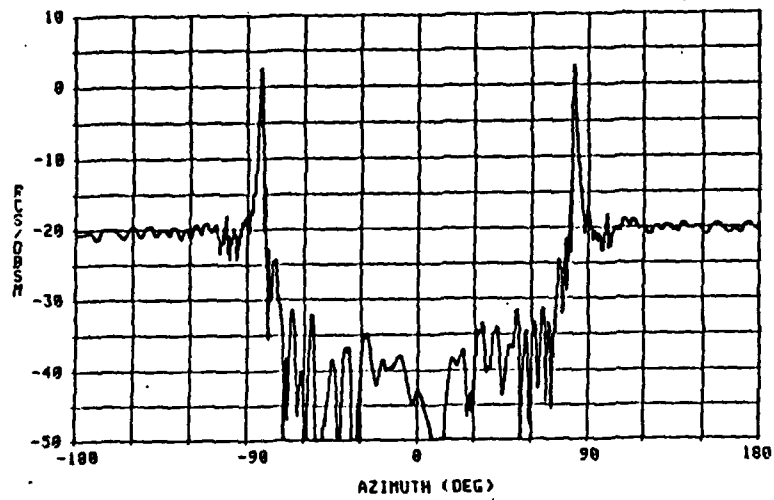


Figure 4.17 CW-Nulling and Pulse-Gating Measurements of a Cone-Sphere
(15 GHz, Vertical Polarization)

MODEL CW CONE-SPHERE AT 18 GHZ
FREQ 18 GHZ FOL UT RANGE 34



MODEL PULSED CONE-SPHERE AT NEW FREQUENCY
FREQ 18 GHZ FOL VE RANGE 34

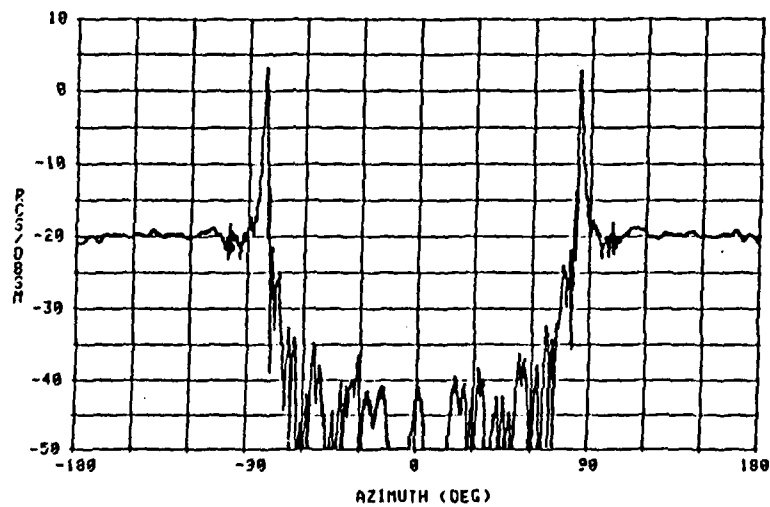
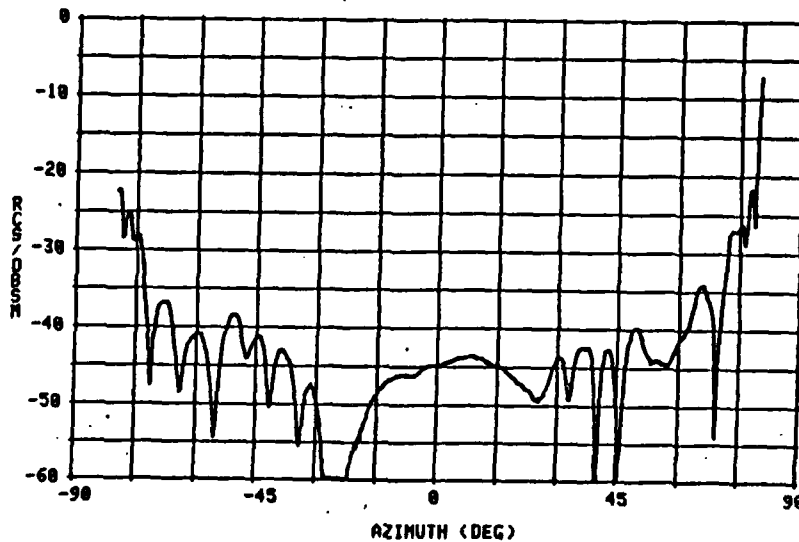
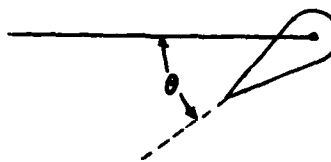


Figure 4.18 CW-Nulling and Pulse-Gating Measurements of a Cone-Sphere
(18 GHz, Vertical Polarization)

reflector, was then nulled at 8.5 GHz with vertical polarization. The cone-sphere was then placed in the chamber and a pattern was measured over $\pm 80^\circ$ off nose-on aspect. The measurement was then repeated using the pulse-gated system. The results of these measurements are shown in figure 4.19. Although the cone-sphere was not properly levelled on the top of the support pedestal resulting in slight deviation from symmetry about zero degrees, there are drastic differences between the CW-nulling and pulse-gated measurements. The forward scattered energy reflects from the corner reflector and interacts with the direct return from the cone-sphere, thereby distorting the pattern. Obviously, corner reflectors are not normally placed in anechoic chamber backwalls, yet a poorly designed backwall can scatter as much energy as a small corner reflector. The point is that the radar receiver doesn't know whether the clutter source is a corner reflector or a poorly constructed backwall: it certainly cannot distinguish a target return from a clutter source return. Therefore it appears that gating out the clutter source contribution to the RCS is superior to compensating for the clutter source return as it totally eliminates the clutter source as a possible contributor to the RCS. This is especially significant when the target RCS is on the same order of magnitude as the other chamber clutter sources.

There is still one feature of the pulse-gated plots that has not yet been discussed. Note that the pulse-gated patterns of figures 4.17 and 4.18 are different even though the target is still the cone-sphere of figure 4.1. The reason for this is because the cone-sphere target, when placed atop the support column, interacts with the column causing multiple bounces and direct coupling with the top of the column that is difficult

MODEL CW CONE-SPHERE, 13 JUNE 1985
FREQ 8.5 GHZ POL V RANGE 45



MODEL PULSED CONE-SPHERE, 13 JUNE 1985
FREQ 8.5 GHZ POL V RANGE 45

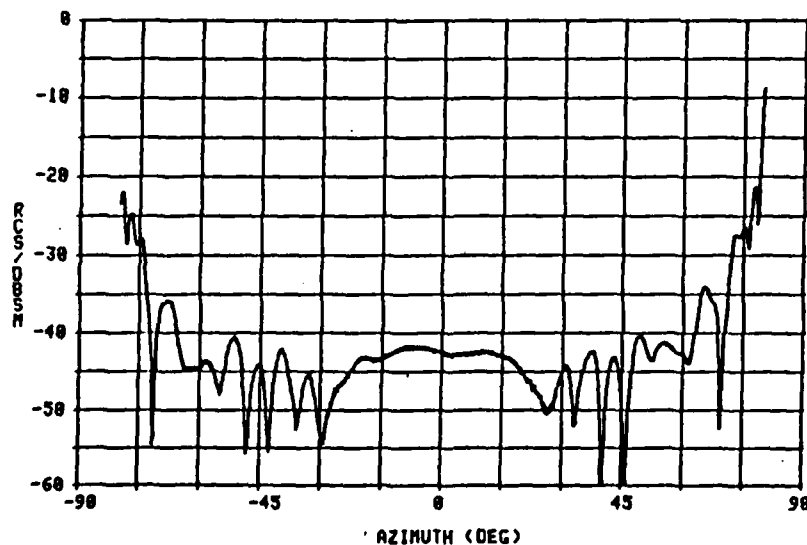


Figure 4.19 CW-Nulling and Pulse-Gating Measurements of a Cone-Sphere With a Small Corner Reflector Embedded in Chamber Backwall

to duplicate in successive measurements. The cone-sphere can never be placed on the column in exactly the same spot and may overhang the column by different amounts, or may be slightly unlevelled from one measurement to the next, or may experience other slight re-positioning errors which cause great difficulty in repeating successive cone-sphere measurements. Unfortunately this coupling can not be gated out nor can it be nulled out with CW-nulling.

Even the target support column itself has a tendency to act as a clutter source. The support column is shown in figure 4.20 and a number of different clutter sources can be seen. The absorber foil or baffle (popularly called a "boat") is designed to shield the turntable motor from the view of the antennas. Due to the abrupt edge termination of this baffle, there can be significant diffraction effects that bring the motor into view. The RCS of this low cross section ogival tower is thus spoiled by the absorber foil that is placed in front of its base. CW-nulling can compensate for this type of clutter but pulse-gating cannot without background subtraction.

To verify that this problem was indeed caused by the baffle, a target support column was brought in that was built differently. This support column, to be used in the new compact range facility described in Appendix C, is shown in figure 4.21. This newer support column has a much lower composite cross section than does the column of figure 4.20. The difference in measured RCS for these columns was about 15 dB, with the new column being lower than the far-field column. Thus it is possible to reduce the effect of target support pedestal interference.

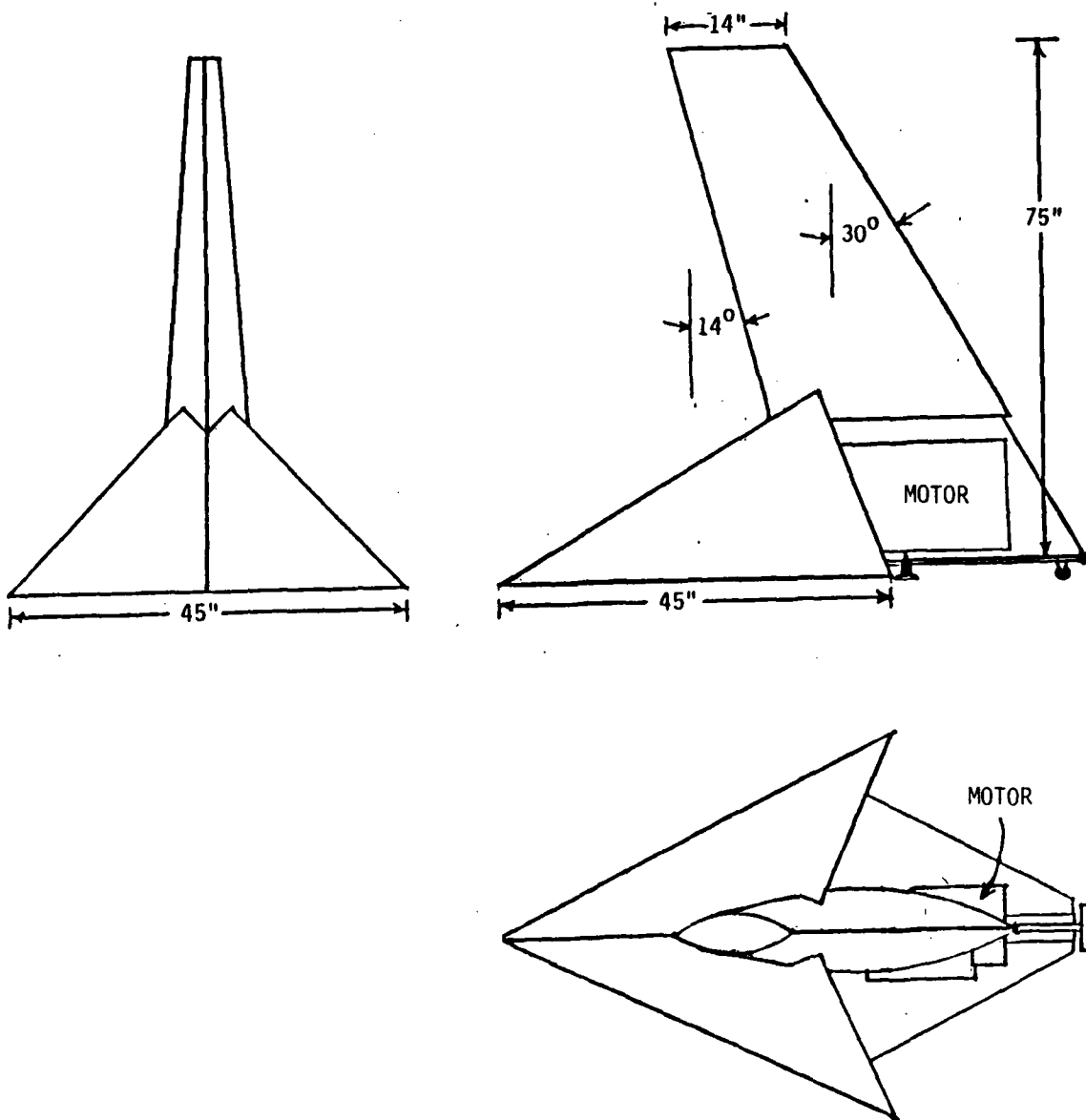


Figure 4.20 Illustrative Diagram of Far-Field Range Low RCS Support Pedestal and Surrounding Features

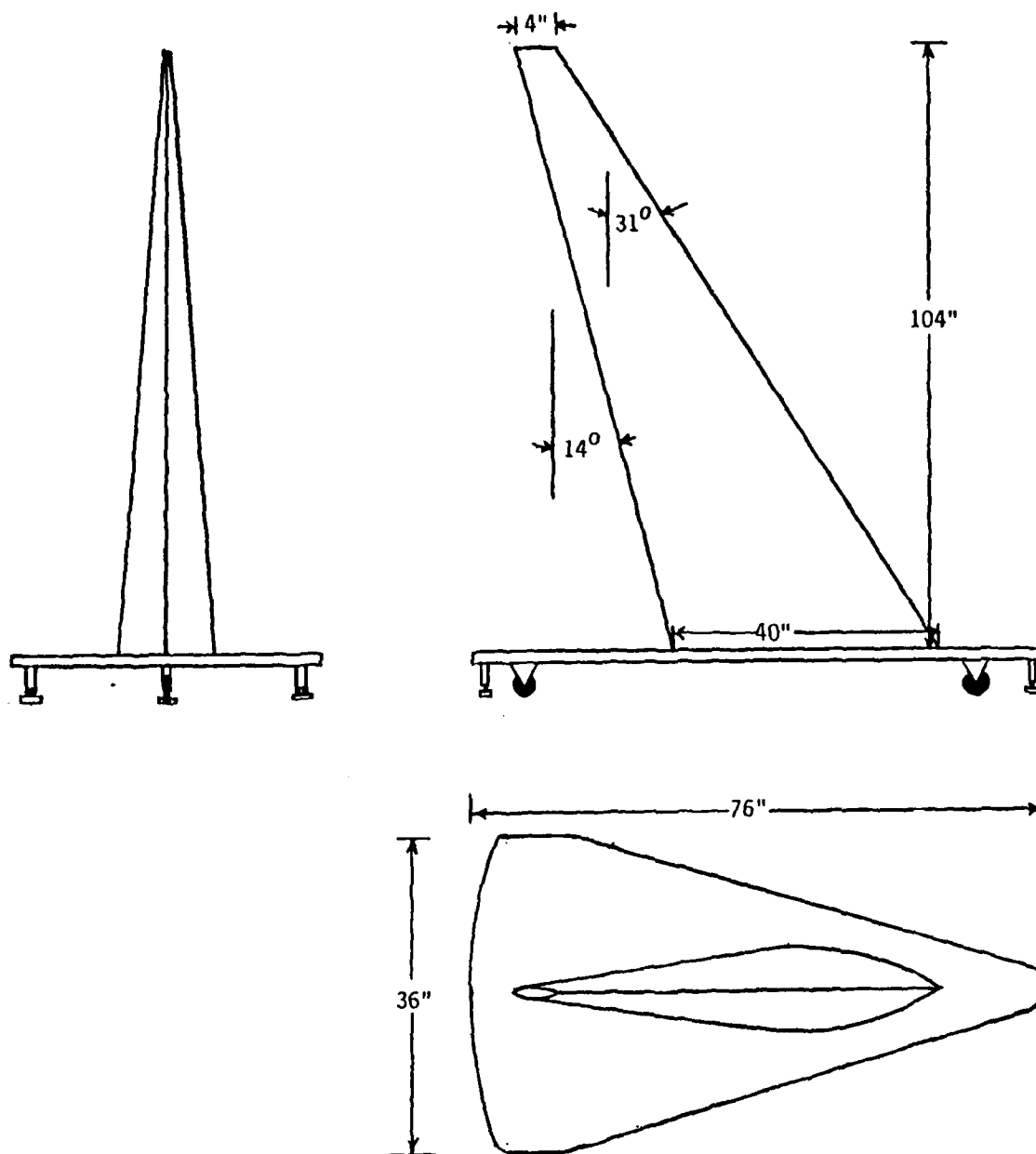


Figure 4.21 Illustrative Diagram of New Compact Range Low RCS Support Pedestal and Surrounding Features

V Conclusions and Recommendations

A. Conclusions

It was the purpose of this thesis to compare the CW-nulling and pulse-gated RCS measurement systems using a communication theory systems approach and show how the background characteristics differ between the two systems. The results of the systems' analysis from Chapter III and the background comparison from Chapter IV can be summarized as follows:

- 1) The CW-nulling system is less complex than the pulse-gating system,
- 2) Pulse-gating has superior system noise figure and is potentially more sensitive than the CW-nulling system,
- 3) The pulse-gating system is less susceptible to chamber background clutter source reflections than is CW-nulling,
- 4) The pulse-gating system yields more accurate measurements of low RCS targets.

To extend the capabilities of an RCS measurement radar system, the elimination or reduction of background clutter is paramount. For this purpose, the pulse-gated system is clearly superior to the CW-nulling system.

In Chapter IV it was mentioned that not all clutter sources could be gated out. This was in reference mainly to clutter from the target support column and the target coupling with the support column. The data presented in Chapter IV indicate that these problems are minor, causing only a problem with measurement repeatability. When the target response

is close to the system noise level as is the response from the cone-sphere, even very minute signal fluctuations become important. Clearly, the results of Chapters III and IV indicate that the pulse-gating system is better capable of dealing with such changes in the background signal.

B. Recommendations

Based on the results of Chapter IV some recommendations will be made concerning the RCS measurement of different target types. There are basically two types of targets; high RCS targets and low RCS targets. High RCS targets refer to targets such as the square plate and cylinder targets used in Chapter IV. These were targets where the specular contribution dominated over diffraction and creeping wave contributions for most aspect angles. Low RCS targets refer to targets such as the cone-sphere which are physically large but have small returns over certain aspect angles. This is where a creeping wave or diffraction contribution dominates over any specular contribution to the RCS. In this case the specular component is directed away from the backscatter direction. There are also physically small targets that have low RCS due to their small size. An example of this is a single chaff half-wave dipole. Although the specular contribution is dominant in the RCS, the dipole is so small that its RCS is low.

For the measurement of high RCS targets either the CW-nulling or pulse-gated systems can be used with confidence. It is not entirely necessary to gate out any chamber clutter sources as the target response will be dominant. This was shown convincingly with the 8 inch sphere in the time domain plots in Chapter IV. It was also very difficult to

distinguish any differences between the CW and pulsed patterns of the square plate and cylinder. Thus it would make no difference which system is used to measure a target like these.

For low RCS targets the pulse-gated system must be used. As seen in figures 4.6 and 4.7 the target return is on the same order of magnitude as the chamber clutter source returns. Obviously these clutter sources must be gated out so that the system response is limited to the target area. If the pulse-gated system is combined with vector subtraction, the accuracy should be increased. Unfortunately there was not time to verify this combination during this study. It is recommended that this combination be tested by AFWAL.

Another recommendation, one that departs from the topic above, is that the pulse-gating and CW-nulling systems be combined on the far-field range. During the first few months of this study we were forced to operate this way due to EMI problems. Once these EMI problems were solved we could operate the pulse-gated system with no clutter canceling mechanism. Due to the tips of the cone absorber lining the chamber sidewalls acting as clutter sources, it became necessary to rearrange the sidewalls of the chamber, moving them as far back as possible. This was because the antennas were illuminating the sidewalls at roughly the 20 dB point on the antenna patterns (see Appendix C, figure C.2 for far-field antenna patterns) which limited the background level to 40 dB below the peak antenna response. Moving the sidewalls back worked fine but left the chamber in a state of being non-anechoic with gaps between sidewall panels, etc. In order to put the chamber back into its original condition and still operate in the pulse-gated mode, it is recommended that the CW-

nulling loop be left in the system to null out these remaining clutter features. This circuit is shown in figure 5.1. This, of course, restricts operation to fixed frequencies, but this is fine for azimuth pattern measurements.

With this system installed, it is possible to gate out clutter sources such as the chamber backwall and null out clutter sources remaining within the range gate such as the sidewalls and the support pedestal. Also, the inclusion of the nulling loop would ease the requirement of EMI proofing of all waveguide joints, etc. This system is recommended for the AFIT RCS chamber, where a flat backwall and close-in sidewalls would limit the effectiveness of either CW-nulling or pulse-gating alone, but could be compensated for by this hybrid system. Combining this with background subtraction should further increase the overall system sensitivity of the AFIT RCS measurement system.

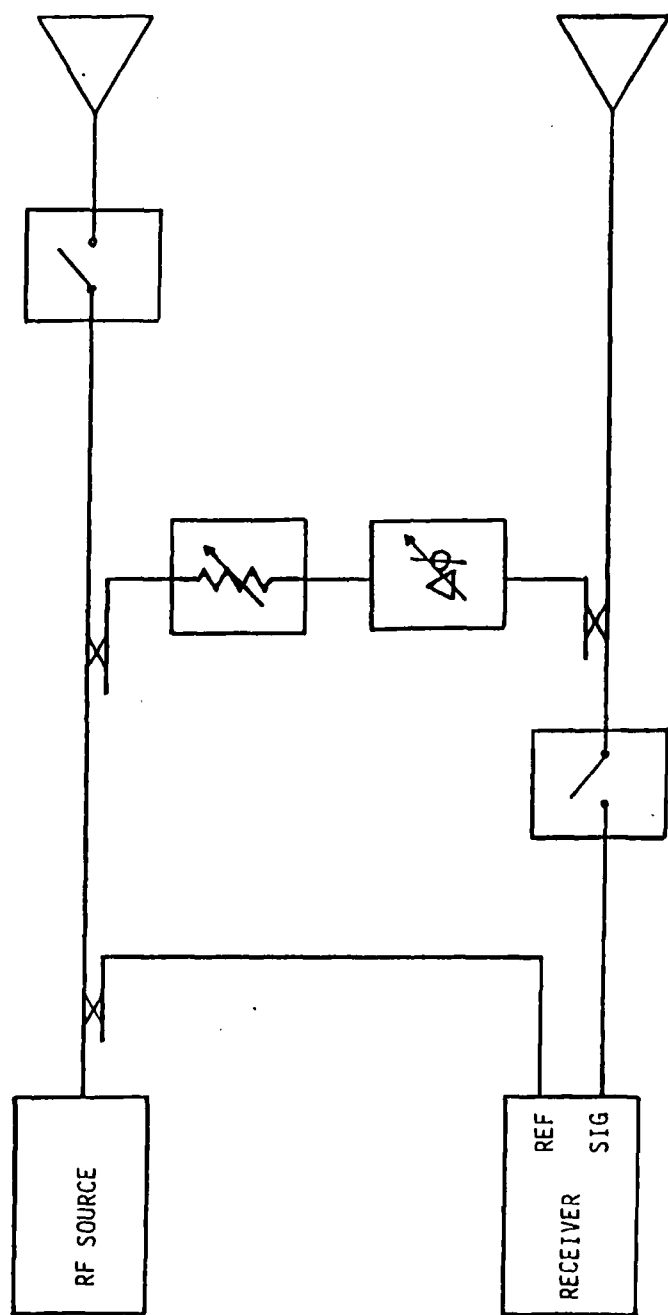


Figure 5.1 Hybrid CW-Nulling/Pulse-Gating System Recommended For Use on AFIT RCS Chamber

Appendix A. Stepped Frequency/Time Domain Measurements

In chapter IV both time domain and fixed frequency measurements were used to characterize the anechoic chamber and/or the various targets of interest. The fixed frequency pattern measurements were capable of providing a 360° plot of the target RCS versus azimuth angle. The time domain plots, on the other hand, show a time history of the scattering within the chamber at a fixed azimuth angle. In the time domain measurements, individual scatterers within the chamber are isolated and target scattering could be visually compared to clutter source scattering. Scattering mechanisms (physical phenomena) could also be isolated provided the initial measurement resolution was sufficient. To properly understand and characterize the chamber described in chapter IV, a detailed knowledge of the scattering sources and mechanisms inside the chamber was required. This information could only be provided through the use of a time domain system.

The basic concept of a time domain system is quite simple, originating from basic Fourier theory. We normally associate Fourier transform concepts with the mapping of a function in the time domain to a function in the frequency domain. To do this with the aid of a computer the function in one domain is sampled or digitized into an ordered sequence and mapped or transformed into the other domain as another sequence. This is called a discrete Fourier transform.

The discrete Fourier transform pairs for an N^{th} order sequence (N being the number of samples comprising the sequence) are expressed as (16:91),

$$G(f) = \frac{1}{N} \sum_{t=0}^{N-1} g(t) \exp\left(-j \frac{2\pi f t}{N}\right), \quad f \in [0, N-1] \quad (A-1)$$

$$g(t) = \sum_{f=0}^{N-1} G(f) \exp\left(j \frac{2\pi f t}{N}\right), \quad t \in [0, N-1] \quad (A-2)$$

where $G(f)$ is the forward transform and $g(t)$ is the inverse transform.

The motivation for the discrete Fourier transform is that $g(t)$ and $G(f)$ can be complicated functions that may not have specific analytical expressions. This is the case with many "real-world" signals and waveforms of current interest and is certainly true for the time history function of the scattering effects and sources within AFWAL's far-field RCS chamber.

To demonstrate the implementation of this technique, suppose the RCS measurement system can obtain coherent RCS data over a reasonably large number of equally spaced frequencies. After acquiring RCS data versus equally spaced frequency increments, we artificially create an even function by reflecting the measured amplitude data about zero frequency. Furthermore, we create an odd function by reflecting the measured phase data about zero frequency and multiplying the negative angular spectrum by -1. This newly created complex frequency spectrum is then Fourier transformed into a real time function. The resulting time function represents a time history of the scattering sources within the entire anechoic chamber. By choosing proper frequency increments and bandwidths, individual scattering mechanisms can be identified. The ultimate resolution in the time domain depends on the frequency increment, the number of sample points, and the bandwidth over which the frequency is taken.

To demonstrate how this technique works refer to figure A.1, which represents a cutaway view of the far-field measurement facility. A target is located 37.5 feet from the antennas and the chamber backwall is 65 feet from the antennas. Suppose that amplitude and phase RCS data is taken at 4 MHz ($\Delta f = 4$ MHz) increments from 8.2 to 12.296 GHz. This equates to 1024 equally spaced frequency data points which gives a measurement bandwidth of 4.096 GHz ($BW = 4.096$ GHz). The measured amplitude and phase data is then reflected about the origin in the manner described above. This process is shown in figure A.2a. The frequency domain data is then Fourier transformed, resulting in the conceptual time domain plot shown in figure A.2b. The highest unambiguous time, (t_{HI}), is related to the frequency increment by

$$t_{HI} = \frac{1}{\Delta f} \quad (A-3)$$

while the time domain resolution, Δt , is related to the bandwidth by,

$$\Delta t = \frac{1}{BW} = \frac{1}{N \Delta f} \quad (A-4)$$

Conceptually, the hypothetical time domain plot shows scattering due to direct transmit/receive antenna crosstalk, the target, and the chamber backwall. There are, however, several implicit assumptions made regarding this conceptual time domain plot. First, it is assumed that no range gating has been used. Second, it is assumed that the bandwidth of the scan provides enough time domain resolution to see the individual chamber scatterers. Third, we assume that the frequency increment, Δf , is chosen small enough to unambiguously discern all aspects of the chamber. For example, if $\Delta f = 10$ MHz the time domain resolution would be 100 nsecs.

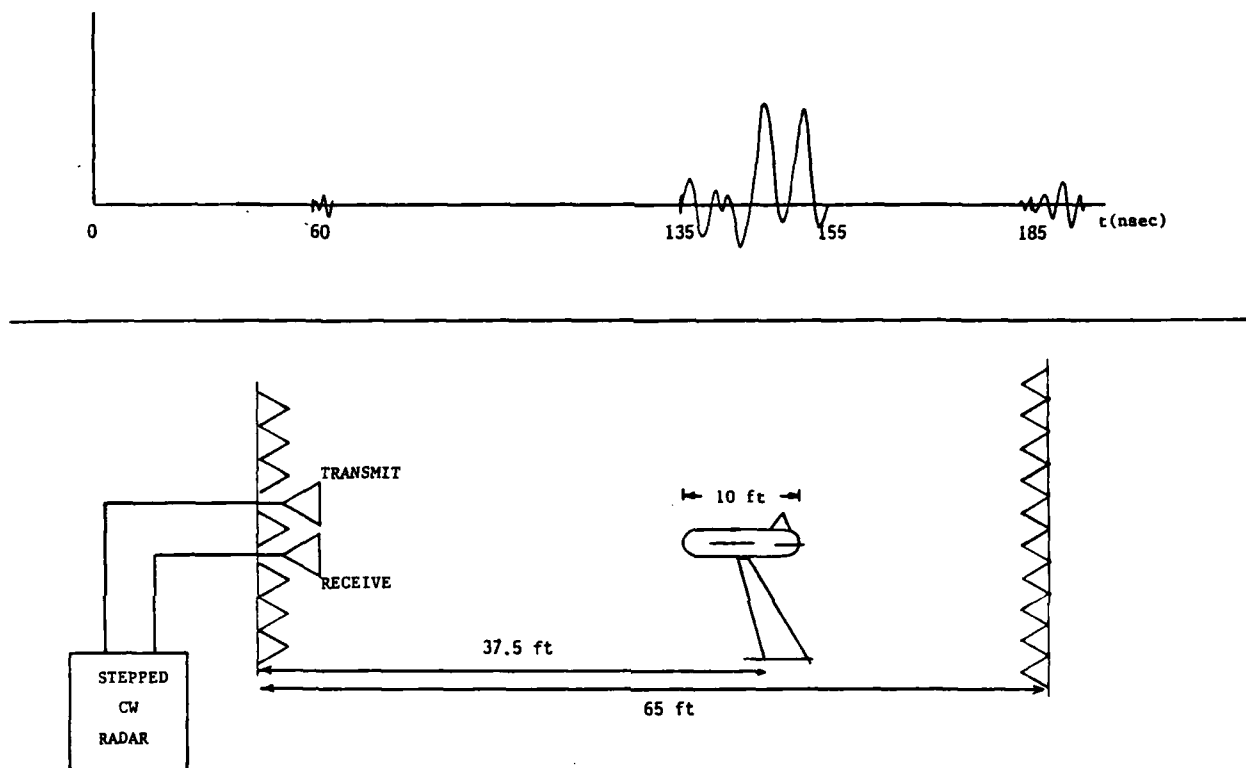
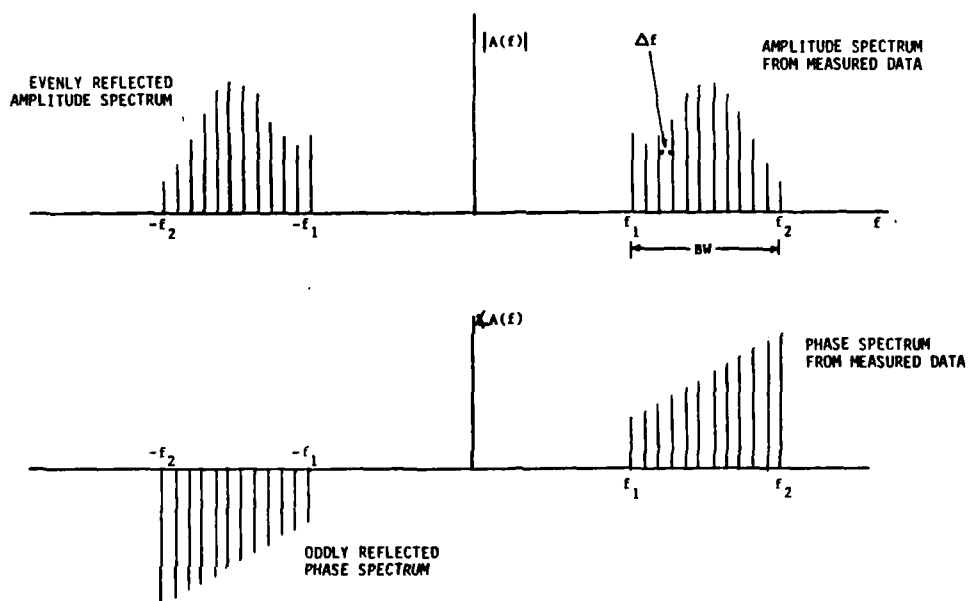
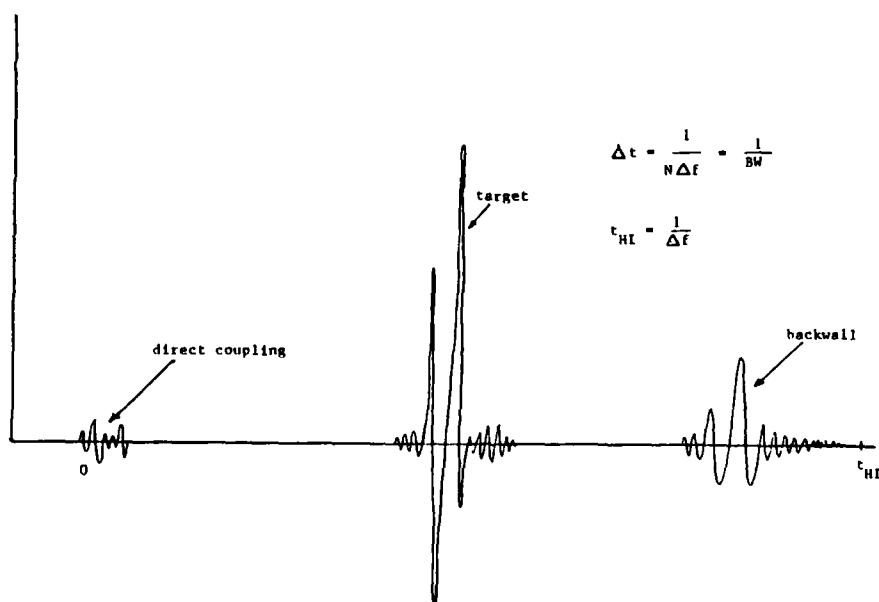


Figure A.1 Cutaway View of Far-Field Range and a Resultant Time Domain Response Scan



(a) Conceptual Frequency Domain Data



(b) Conceptual Time Domain Data

Figure A.2

If a target resided 65 feet (roughly 130 nsec) from the radar transmitter, the time domain plot would "wrap around" to 30 nsec due to frequency aliasing. If $\Delta f = 5$ MHz were chosen instead, the unambiguous time would be increased to 200 nsec, and the target response would properly appear at 130 nsec. Finally, no attempt was made to account for spurious effects caused by sampling in frequency over a finite bandwidth. Usually, data taken over a finite bandwidth is adjusted by weighting the measured spectra with a Hanning window function (7:1222). This reduces the Gibbs phenomena effect caused by transforming band-limited data.

Any equipment error that occurs during the measurement of the frequency domain data can cause distortion in the resultant time domain plot. For instance, several times during this investigation, false frequency domain data was recorded. In figure 4.2, several bad data values were transformed into the time-domain (less than 5 out of 512 samples). The resultant ringing is noticeable between the target, the control cables, and the backwall. Low level ringing can even occur when as few as one or two bad data points are transformed as seen in figures 4.3 and 4.10. The potential of a totally unrecognizable plot occurs when there are a high number of bad data points transformed. Figure A.3 shows the result of transforming about 10 such data points into the time domain.

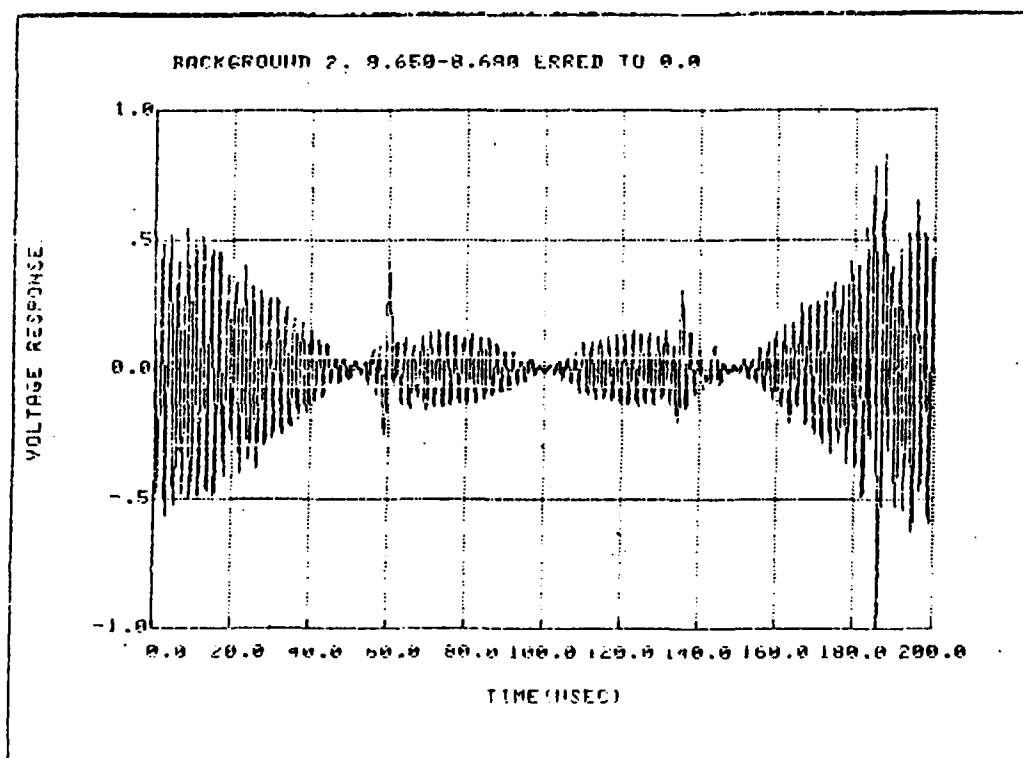


Figure A.3 Sample Results of Transforming Bad Frequency Domain Data Into the Time Domain

Appendix B: Fundamental Mode Mixing

In chapter IV it was very briefly mentioned that a fundamental mode mixing (FMM) scheme was tried in an effort to increase the sensitivity of the pulse-gated system. This experiment occurred towards the end of this study and, unfortunately, was not fully completed. But the results that were obtained are encouraging. It is the purpose of this appendix to include in this thesis pertinent information and discussion concerning FMM, as it appears to be a viable technique for increasing the system sensitivity of the pulse-gated RCS measurement system.

The basic FMM system is shown in a simplified block diagram in figure B.1. The FMM system employs two WJ 1250A frequency synthesizers, one used as the RF source and the other used as a precision local oscillator. The difference frequency is chosen to lie within the fundamental frequency range (fundamental mode) of the SA 1750 (or SA 1780) receiver's first local oscillator. This local oscillator can only be tuned from 2 GHz to 4.1 GHz in the case of the SA 1750 (from 1 GHz to 2 GHz in the SA 1780). The SA harmonic mixer generates harmonic signals in its crystal element that are strong enough to downconvert to the 45 MHz IF incoming signals that are harmonically related to the fundamental mode. As the incoming signal frequency becomes farther removed from the fundamental mode, the appropriate harmonic signal used to downconvert to IF becomes weaker in amplitude. Thus a mixer conversion loss is associated with each of these harmonics of the fundamental. Table B.1 shows the frequency ranges and their associated receiver sensitivities. Note that the sensitivity decreases for increasing frequency. This decrease in sensitivity is

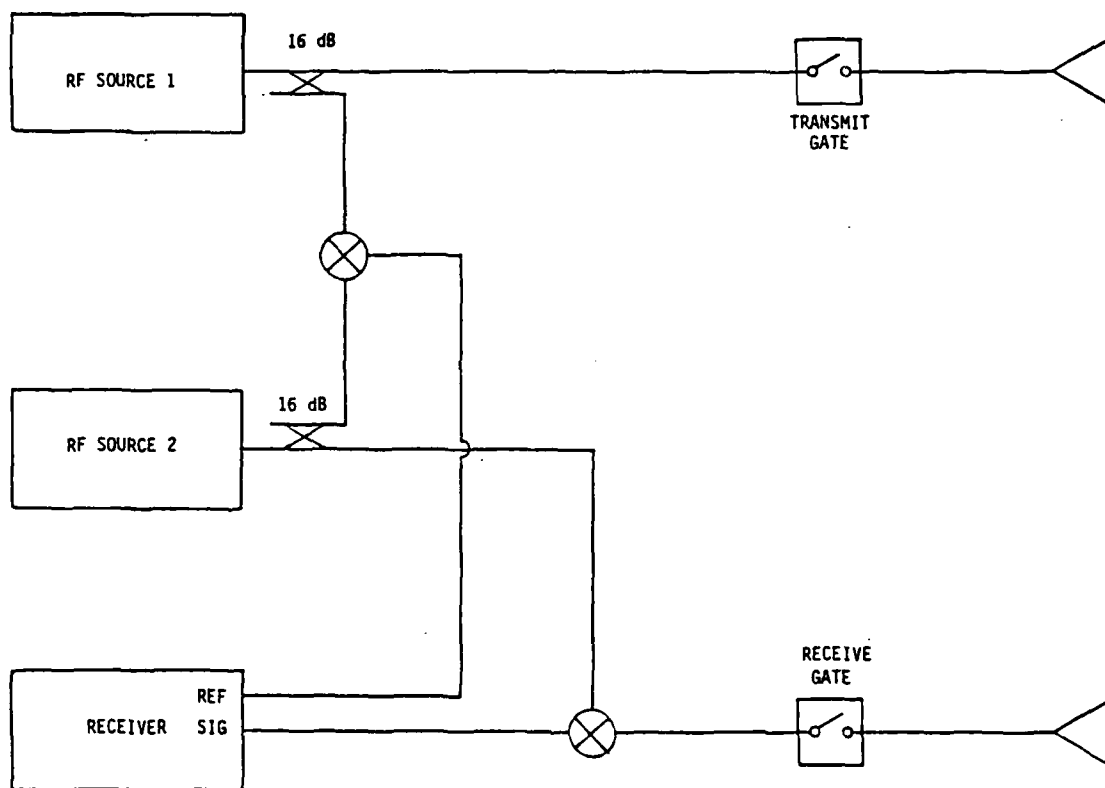


Figure B.1 Simplified Diagram of Fundamental Mode Mixing System
(With Pulse-Gating System)

Frequency Range (GHz)	Signal Channel Sensivity (dBm)
2 - 4	-120
4 - 8	-115
8 - 12	-110
12 - 18	-105
18 - 26	-100
26 - 40	- 90

Table B.1 SA 1750 Receiver Sensitivity Characteristics Due to
Harmonic Mixer Front End

attributed entirely to mixer conversion loss (12).

Thus, the signal returned from the chamber is downconverted to the fundamental mode of the receiver's first conversion stage. As shown in Table B.1, the sensitivity of the SA 1750 in the fundamental mode is -120 dBm. Stepping up into the next frequency band incurs a conversion loss of 5 dB in the mixer, and into yet the next band, an additional 5 dB of mixer conversion loss. If the test signal seen by the harmonic mixer is in the fundamental mode, then no conversion loss occurs. By downconverting a test signal prior to reaching the harmonic mixer, the only conversion loss suffered would be that of the added mixer. Obviously this new mixer should be of a different type, and should have less conversion loss than the harmonic mixer at the operating frequency. This is the motivation and purpose of FMM; regaining a part of the conversion loss when operating in the X-band or higher.

In the practical implementation of this technique at AFWAL, Anzac (Adams-Russell) MDC-167 High IF Double-Balanced microwave mixers were used as the FMM mixers. Note that the resultant fundamental mode is the IF product of this mixing operation (see figure B.1). Specifications for the MDC-167 indicate that for an IF of 2 GHz, the average conversion loss is 8 dB. So for X-band, a 2 dB improvement in sensitivity is expected while for Ku-band, a 7 dB improvement would be expected. This particular mixer (the MDC-167) would have to be replaced with a higher frequency mixer for operation above 18 GHz. This would also necessitate a recalculation of the expected improvement in sensitivity since a higher frequency mixer could have a higher conversion loss.

From the discussion above, it would be unwise to implement a FMM

AD-A163 965

COMPARISON OF BACKGROUND CHARACTERISTICS OF AN RCS
(RADAR CROSS SECTION)... (U) AIR FORCE INST OF TECH
WRIGHT-PATTERSON AFB OH SCHOOL OF ENGI... G R SIMPSON
DEC 85 AFIT/GE/ENG/85D-48 F/G 1779

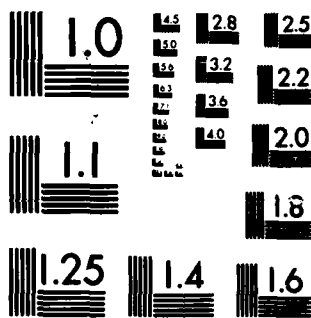
2/2

UNCLASSIFIED

NL

END

FILED
in
GTC



MICROCOPY RESOLUTION TEST CHART
NATIONAL BUREAU OF STANDARDS-1963-A

modification if the operating frequency is not in the X-band or higher. Maximum sensitivity occurs in the fundamental mode as shown in Table B.1. So this method is limited to higher frequency measurements.

The major problem with this scheme is EMI. RF shielded enclosures were constructed for the double-balanced mixers. These enclosures were also stuffed with scrap dielectric absorber. When this technique was attempted without RF shielding of the mixers, direct coupling into the mixers rendered the entire setup useless. EMI precautions are an absolute must when this technique is combined with pulse-gating. FMM and CW-nulling have not yet been tried in combination at AFWAL, but the mixers may be so prone to direct coupling that the nulling loop may prove ineffective in cancelling the direct signal.

Beyond these EMI precautions, no problems with the FMM system were noted. Unfortunately, in the time allowed, we never were able to operate above 12 GHz so only marginal (~2 dB) improvements were noted. Operating above 12 GHz should yield 7 dB improvement, but this performance will have to be verified by another worker.

Appendix C: Some Comments on Differences Between the Compact Range and the Far-Field Range

In the introduction to this thesis it was stated that the interest in the compact range was partially motivated by a desire to keep with the state of the art in RCS measurements. There are a number of reasons why the trend today is toward the compact range facility. The compact range utilizes a large paraboloidal reflector antenna that is offset-fed by a horn antenna located at the reflector focus. This produces a collimated beam that in the aperture plane and projecting outward is a uniform plane wave. With this facility, larger targets can be measured indoors at a relatively short range without violating the traditional far-field criteria. Illumination of chamber clutter sources is less than in the far-field range. Clutter sources like the chamber sidewalls and the base of the target support column have proven to be troublesome in the far-field range but would not be illuminated as strongly in the compact range. Additionally, return from these off-axis clutter sources would not reflect as strongly into the compact range receive feed horn as they might reflect into a far-field range receive antenna. This is because of the formation of confocal surfaces for off-axis illumination that do not converge or fully intercept the reflector focus. These are just a few of the advantages of the compact range facility.

Figure C.1 is a simplified conceptual diagram of the compact range. The beam collimating property of the paraboloidal antenna forms, as mentioned above, an area of plane wave illumination called a quiet zone. The size or extent of a target is limited only by the size of this quiet

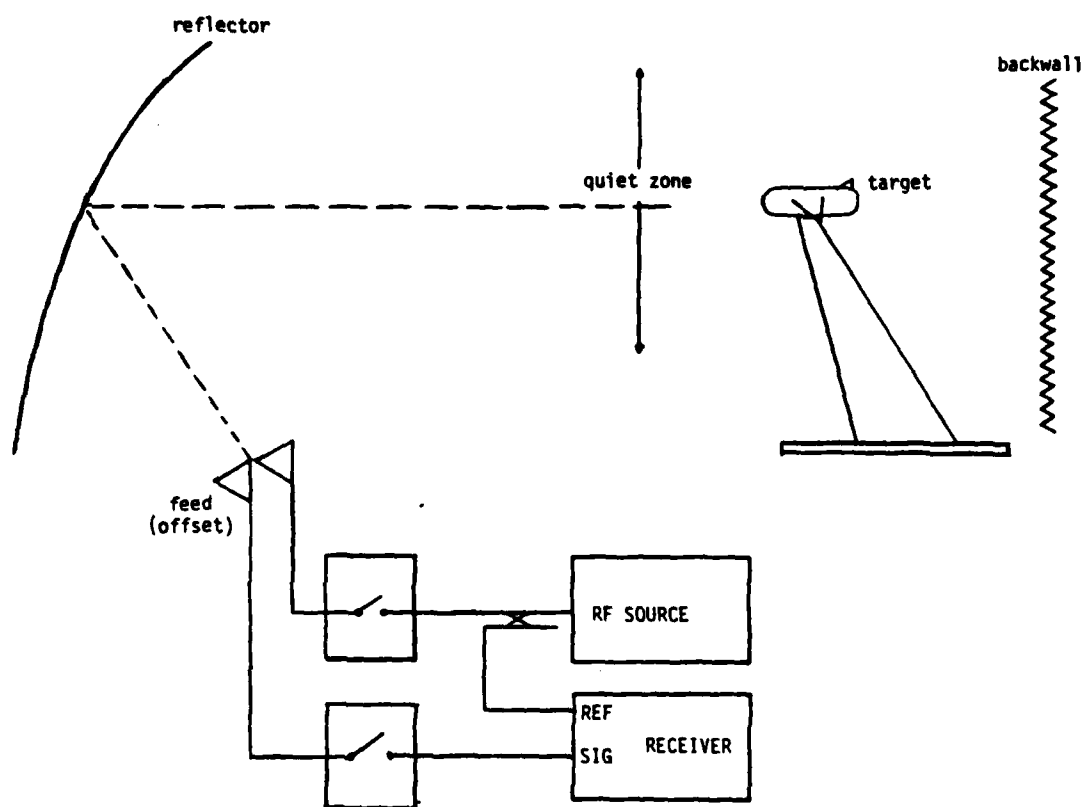


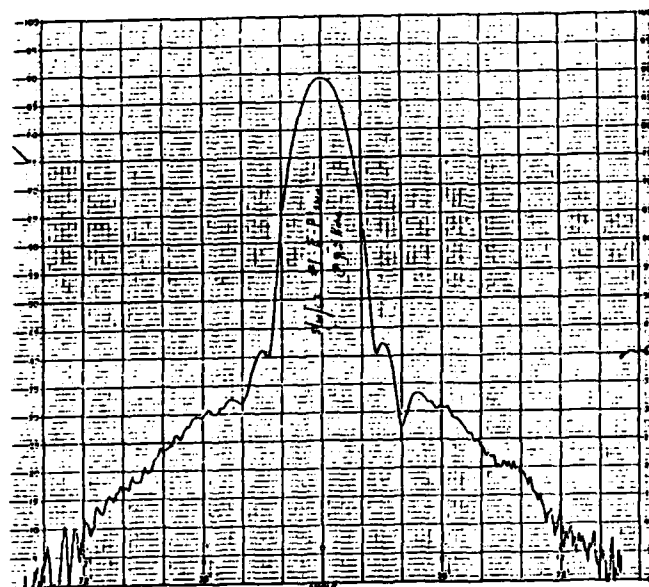
Figure C.1 Simplified Diagram of Compact Range Geometry

zone. The size of the quiet zone is proportional to the size of the reflector and is dependent on how well edge diffraction effects (caused by the edges of the reflector) are suppressed (17). This last effect is why many compact range reflectors are modified with an elliptically rolled edge termination. Diffraction phenomena then occur harmlessly on the backside of the reflector and energy incident of the modified edge (just off the parabolic surface) are specularly directed away from the quiet zone (17).

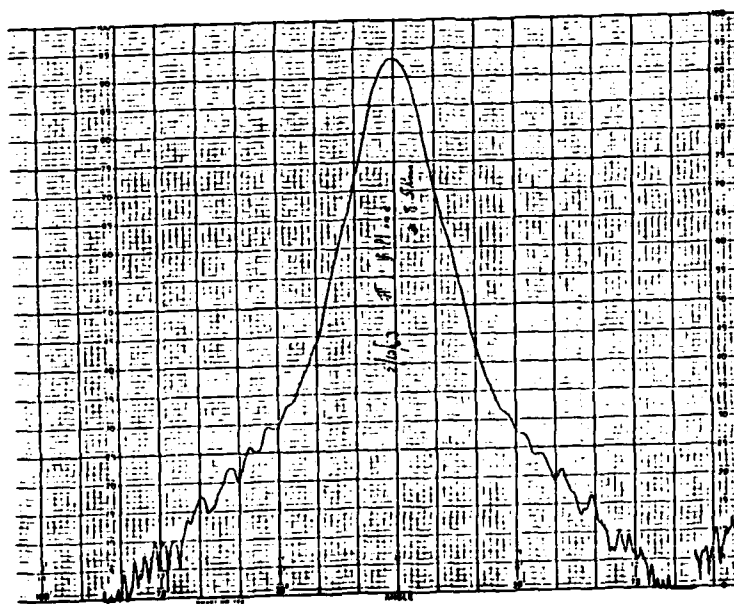
Typical far-field ranges have antenna patterns as shown in figure C.2. To satisfy the far-field criterion of $\lambda/8$ maximum phase variation across the measured target surface requires the familiar range relation of

$$R > \frac{2D_1 D_2}{\lambda} \quad (C-1)$$

where D_1 and D_2 are the maximum linear extent of the antenna and target respectively. Another far-field criterion is that there be less than 1 dB of amplitude variation over the measured target surface. By applying equation (C-1) to a 9.5 GHz measurement of a target at a range of 45 feet, we see that the far-field range antenna illumination restricts the size of target models that can be measured to roughly 18 inches in maximum linear extent (transmit antenna aperture is also 18 inches wide). The compact range, with its large quiet zone, is not so restrictive, nor does it take up the same linear space as required by equation (C-1), even for relatively small wavelengths. As an example, a target five feet in extent is measured on the far-field range at 18 GHz. The antenna aperture dimension for this frequency is 14 inches. Equation (C-1) requires a range of over 183 feet to satisfy the far-field criteria.



(a) E-plane, 9.5 GHz



(b) H-plane, 8.5 GHz

Figure C.2 Sample Far-Field Antenna Radiation Patterns

The quiet zone projecting out from the reflector is, to a first order approximation, determined by simple geometrical optics. The field outside this region is, to this same order approximation, zero. Obviously this is not the case as is discussed above and in reference (17). A typical antenna pattern for a compact range reflector is shown in figure C.3 (17). This is a vertical pattern cut but it is representative of the amplitude taper beyond the quiet zone on a reflector that has the rolled edge modification. The amplitude taper from the edge of the reflector is about 9 dB in 24 inches or 4.5 dB per ft. The far-field range antenna patterns have a taper of about 2 dB per ft. (see figure C.2). This is how the compact range illuminates sidewalls and other clutter sources less strongly than do the far-field range antennas.

Recall in Chapter IV that the pulse-gated system was still subject to clutter caused by the target support column. On the far-field range, the lower part of the column was illuminated nearly as strongly as the target on top of the column (see figure 4.21). In the compact range, the lower part of the column is illuminated much less strongly than is the target in the quiet zone. Naturally we would expect the clutter levels to be that much less if this column were used on the compact range. Better still, the column to be used in the AFWAL compact range, shown in figure 4.22, is of a superior mechanical design from the point of view of as a clutter source contributor. The direct clutter from this column is caused mainly by the casters, levelling feet, and the edge of the base that is seen by the incident field. This area is easily treated with several pieces of absorber and the clutter level can be reduced by yet another 15 dB. Thus the compact range actually has a lower useable background level than does

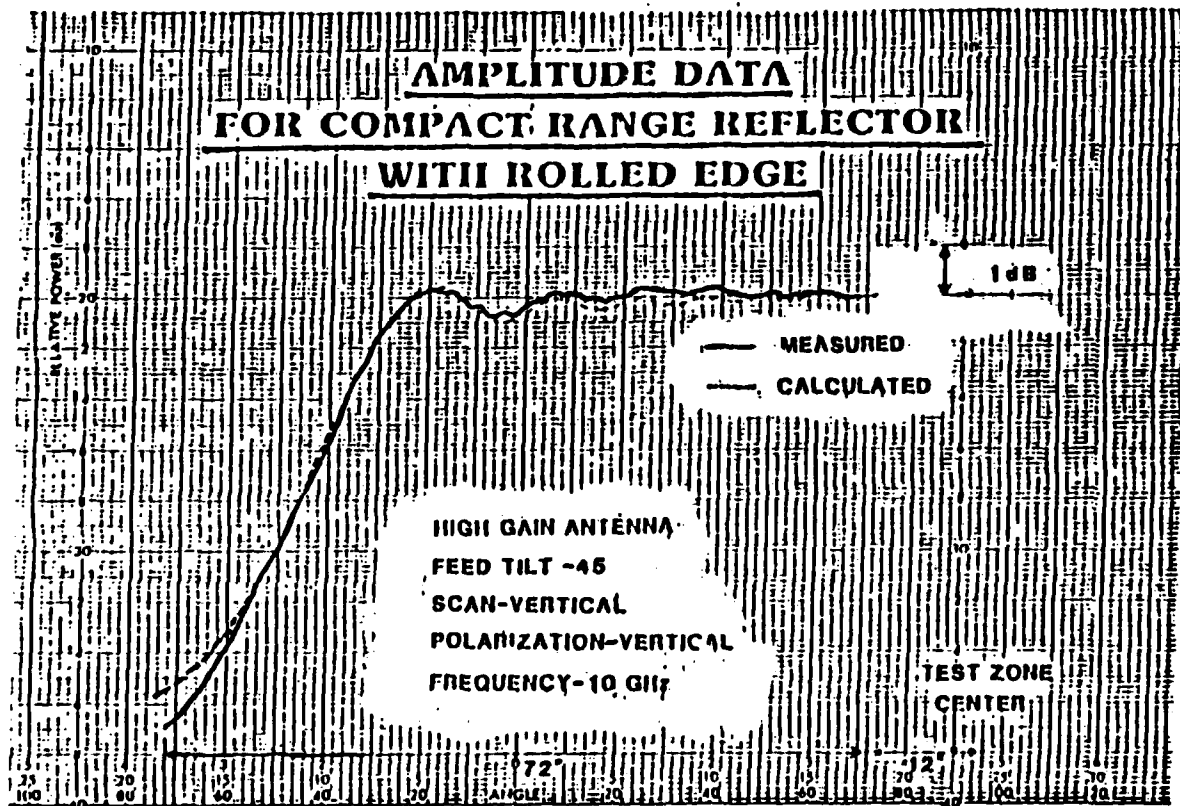


Figure C.3 Sample Compact Range Antenna Amplitude Distribution
(Adapted from Reference 17)

the far-field range.

In summary then, when the compact range is combined with the pulse-gating radar system, the target area is separated from the chamber environment in two ways. It is range gated by the pulse-gating action of the measurement system and it is spatially gated by the illumination properties of the compact range reflector. Of course this last item is debatable as this spatial gating is not as well defined as the range gate but it is unquestionable that the quiet zone is much more well defined than it is on the far-field range. This spatial gating would certainly be dependent on how steeply the amplitude is tapered in figure C.3.

Bibliography

1. Mentzer, J.R. Scattering and Diffraction of Radio Waves. New York: Pergamon Press, 1955
2. Bahret, William F. "Comments on Static Radar Reflectivity Measurement Techniques," Proceedings of the RADC Radar Cross Section Measurement Symposium, 25-36. RADC-TR-64-25, 1964
3. Blacksmith, P. Jr., R.E. Hiatt and R.B. Mack. "Introduction to Radar Cross Section Measurements," Proceedings of the IEEE, 53: 901-920 (August 1965)
4. Tavormina, Joseph. "Instrumentation Radars Fulfill Role in RCS Measurements," MSN & CT, 15 No. 2: 75-96 (February 1985)
5. Peebles, Peyton Z. Communication System Principles. Reading, Mass. Addison-Wesley, 1976
6. Whitacre, Robert T. The OSU Pulse/CW Radar for Compact Range Radar Cross Section Measurements. MS Thesis, The Ohio State University, Columbus OH, 1985
7. Walton, Eric K. and J.D. Young. "The Ohio State University Compact Radar Cross-Section Measurement Range." IEEE Transactions on Antennas and Propagation, AP-32: 1218-1223 (November 1984)
8. Link, Jon N. Accuracy Estimate for Radar Cross Section Measurements of Targets Modelled by Multiple Independent Scatterers in Constant Clutter. MS Thesis. School of Engineering, Air Force Institute of Technology (AU), Wright-Patterson AFB OH, Dec 1983
9. Skolnik, Merrill I. Introduction to Radar Systems (Second Edition) New York: McGraw-Hill, 1980
10. Instruction Manual, Series 1750 Phase/Amplitude Receivers. Scientific-Atlanta, Inc. Atlanta 1969
11. Instrumentation Products Catalog 1981. Scientific-Atlanta, Inc., Atlanta, 1981
12. Currie, Charles. Principal Engineer, Telephone Conversation. Scientific-Atlanta, Inc. Atlanta, 1985
13. Castor, Maj Kenneth. Course Notes in EE 5.35, Radar Systems Analysis. School of Engineering, Air Force Institute of Technology (AU), Wright-Patterson AFB OH, January 1985
14. Coaxial & Waveguide Measurement Accessories Catalog and Microwave Measurement Handbook. Hewlett-Packard Co., Palo Alto CA, 1982

15. Kent, Brian M. and 1Lt George R. Simpson, "The AFWAL Compact Range Experience," Measurement, Processing and Analysis of Radar Target Signatures. A workshop presented by Ohio State University. Columbus OH, September 1985
16. Weaver, H. Joseph. Applications of Discrete and Continuous Fourier Analysis. New York: John Wiley & Sons, 1983.
17. Burnside, W.D., et al. "Curved Edge Modification of Compact Range Reflector", Submitted for Publication to IEEE Transactions on Antennas and Propagations, 1985.

VITA

First Lieutenant George R. Simpson was born on 14 November 1958 in Cincinnati, Ohio. He graduated from high school in Mt. Orab, Ohio in 1977 and entered the University of Kentucky from which he received the degree of Bachelor of Science in Electrical Engineering in December 1981. Upon graduation, he received a commission in the USAF through the ROTC program. He entered active duty in February 1982 as an electronics engineer in the Parametrics Data Base Branch, Automated Data Base Division, Directorate of Electronic Warfare Data Research, Air Force Electronic Warfare Center, Kelly AFB, Texas. He entered the School of Engineering, Air Force Institute of Technology, in May 1984.

Permanent address: 13439 Lake Grant Road
Mt. Orab, Ohio 45154

UNCLASSIFIED

SECURITY CLASSIFICATION OF THIS PAGE

REPORT DOCUMENTATION PAGE

1a. REPORT SECURITY CLASSIFICATION UNCLASSIFIED			1b. RESTRICTIVE MARKINGS		
2a. SECURITY CLASSIFICATION AUTHORITY			3. DISTRIBUTION/AVAILABILITY OF REPORT Approved for public release; distribution unlimited.		
2b. DECLASSIFICATION/DOWNGRADING SCHEDULE					
4. PERFORMING ORGANIZATION REPORT NUMBER(S) AFIT/GE/ENG/85D-40			5. MONITORING ORGANIZATION REPORT NUMBER(S)		
6a. NAME OF PERFORMING ORGANIZATION School of Engineering		6b. OFFICE SYMBOL (If applicable) AFIT/ENG		7a. NAME OF MONITORING ORGANIZATION	
6c. ADDRESS (City, State and ZIP Code) Air Force Institute of Technology Wright-Patterson AFB, Ohio 45433				7b. ADDRESS (City, State and ZIP Code)	
8a. NAME OF FUNDING/SPONSORING ORGANIZATION Avionics Laboratory		8b. OFFICE SYMBOL (If applicable) AFWAL/AAWP-3		9. PROCUREMENT INSTRUMENT IDENTIFICATION NUMBER	
8c. ADDRESS (City, State and ZIP Code) Air Force Aeronautical Laboratories Wright-Patterson AFB, Ohio 45433				10. SOURCE OF FUNDING NOS.	
				PROGRAM ELEMENT NO.	PROJECT NO.
11. TITLE (Include Security Classification) See Box 19					
12. PERSONAL AUTHOR(S) George R. Simpson, B.S.E.E., 1st Lt, USAF					
13a. TYPE OF REPORT MS Thesis		13b. TIME COVERED FROM _____ TO _____		14. DATE OF REPORT (Yr., Mo., Day) 1985 December	
15. PAGE COUNT 106					
16. SUPPLEMENTARY NOTATION					
17. COSATI CODES			18. SUBJECT TERMS (Continue on reverse if necessary and identify by block number)		
FIELD	GROUP	SUB. GR.	Instrumentation Radar Radar Cross Section (RCS) Measurements Anechoic Chamber		
14	02				
19. ABSTRACT (Continue on reverse if necessary and identify by block number)					
Title: COMPARISON OF BACKGROUND CHARACTERISTICS OF AN RCS MEASUREMENT RANGE USING A CW-NULLING TECHNIQUE AND A PULSE-GATING TECHNIQUE					
Thesis Chairman: Randy J. Jost, 1Lt, USAF Instructor of Electrical Engineering					
Approved for public release: 1AW AFR 190-1/					
LYNN E. WOLAVER 16 JAN 86 Dean for Research and Professional Development Air Force Institute of Technology (AFIT) Wright-Patterson AFB OH 45433					
20. DISTRIBUTION/AVAILABILITY OF ABSTRACT UNCLASSIFIED/UNLIMITED <input checked="" type="checkbox"/> SAME AS RPT. <input type="checkbox"/> DTIC USERS <input type="checkbox"/>			21. ABSTRACT SECURITY CLASSIFICATION UNCLASSIFIED		
22a. NAME OF RESPONSIBLE INDIVIDUAL Randy J. Jost, 1Lt, USAF			22b. TELEPHONE NUMBER (Include Area Code) 513-255-3576		22c. OFFICE SYMBOL AFIT/ENG

19 continued

This thesis compares the relative performance of a CW-nulling technique versus a pulse-gating technique for radar cross section (RCS) measurements. The purpose is (1) to provide a detailed comparison of these two systems in terms of system noise figure and systems losses, and (2) to demonstrate the effectiveness of time-separating the target area from the surrounding chamber when using the pulse-gating technique.

The pulse-gating system is shown to have far superior system noise figure characteristics than the CW-nulling system. Pulse-gating has only a slightly greater system loss due to the added complexity of the pulse modulating and range gating components. The combined effect is that the pulse-gating technique is capable of improving signal-to-noise, thus increasing the reliability of making accurate RCS measurements.

It is also shown that the pulse-gating system reduces the effect of chamber clutter sources. Supporting data in the form of moderate resolution time domain measurements of chamber scattering sources is presented. Supplemental fixed frequency target RCS measurements correlate with the time domain results. For high RCS targets where the target return is the dominant chamber scattering mechanism, the systems perform equally well. However, when the target RCS is of the same order as chamber clutter, the CW-nulling system yields distorted results since it fails to distinguish between target and clutter source return. In contrast, the pulse-gating system eliminates the most significant clutter source returns and produces more accurate RCS patterns.

END

FILMED

386

DTIC